Quasi-Real Photo-Production and Semi-Leptonic Decay of D^{*-} Mesons

VRIJE UNIVERSITEIT

Quasi-Real Photo-Production and Semi-Leptonic Decay of D^{*-} Mesons

ACADEMISCH PROEFSCHRIFT

ter verkrijging van de graad van doctor aan
de Vrije Universiteit Amsterdam,
op gezag van de rector magnificus
prof.dr. T. Sminia,
in het openbaar te verdedigen
ten overstaan van de promotiecommissie
van de faculteit der Exacte Wetenschappen
op donderdag 3 maart 2005 om 15.45 uur
in het auditorium van de universiteit,
De Boelelaan 1105

door

Armen Laziev

geboren te Yerevan, Armenië

promotor:	prof.dr.ing. J.F.J. van den Brand
copromotor:	dr. W.H.A. Hesselink

Contents

1 Introduction **1**

2 Deep-Inelastic Lepton-Nucleon Scattering **5**

2.1 Introduction 5

2.2 Kinematical variables 5

2.3 Inclusive Deep-Inelastic Scattering 7

2.4 The Quark-Parton Model 9

2.5 Semi-inclusive Deep-Inelastic Scattering 10

2.5.1 Cross sections in semi-inclusive DIS 10

2.5.2 The double-spin asymmetry in semi-inclusive DIS 12

2.6 Charmed Quarks Created in Photon-Gluon Fusion 13

2.6.1 Double-spin asymmetry in photon-gluon fusion 14

2.6.2 Formation of charmed hadrons near threshold 15

2.6.3 Additional production mechanisms for charmed hadrons 17

2.6.4 Decay of the D^{*-} meson 19

3 Monte Carlo Simulations **23**

3.1 Introduction 23

3.2 The programs AROMA and PYTHIA 24

3.3 Monte Carlo Simulations 24

3.3.1 Analysis of Monte Carlo data calculated with AROMA 24

3.3.2 Analysis of Monte Carlo data calculated with PYTHIA 26

3.3.3 Strategy in the analysis of the Monte Carlo data 28

3.3.4 Mass-difference spectra 30

4 The HERMES Experiment **37**

4.1 Introduction 37

4.2 The HERA electron-proton collider 37

4.3 Internal gas target 39
4.4 The HERMES spectrometer 40
4.5 Tracking detectors 41
4.6 HERMES Particle Identification Detectors 42
4.7 The Luminosity Monitor 46
4.8 Trigger and Data Acquisition 48

5 Data Analysis **51**
5.1 Introduction 51
5.2 Data selection 52
5.3 Vertex reconstruction 54
5.4 Data selection using the results of the Monte Carlo Calculations 55

6 Results and Discussion **63**
6.1 Extraction of the number of events from D^{*-}-decay 63
6.2 Double-spin asymmetry 67
6.3 Discussion 72

7 Summary **77**

8 Samenvatting **81**

Acknowledgements **85**

Chapter 1

Introduction

Deep-inelastic lepton-nucleon scattering (DIS) experiments have shown that nucleons are composed of point-like particles. It was measured in these experiments that the cross-sections only weakly depend on the transferred four-momentum. This result was interpreted as elastic scattering of the lepton from a parton in the nucleon. These partons were already predicted by Gell-Mann[1] and Zweig[2] and named quarks. The first model, with which the properties of the baryons and mesons with smallest mass could be described, contained three quarks and their anti-quarks, namely u ($\bar{u}$), d ($\bar{d}$) and s ($\bar{s}$). Later the model was extended and the c, b and t and their anti-quarks were added.

The model with which the first DIS experiments were described was named the quark-parton model (QPM). In this model DIS lepton-nucleon scattering is characterized by two structure functions, which depend on a dimensionless quantity named the Bjorken scaling variable x [3]. This variable represents the fraction of the nucleon momentum carried by the quarks in a specific coordinate system named Breit frame. A more systematic study of DIS lepton-nucleon scattering showed that the quarks could not account for the total nucleon momentum. The missing part was attributed to the gluons, which have spin-1. The interaction between the spin-$\frac{1}{2}$ quarks and the spin-1 gluons is described in QCD (Quantum Chromo Dynamics). With this theory many properties of hadrons and mesons, which are composed of three quarks and a quark anti-quark pair, respectively, and their interactions are described successfully. The contributions of the valence quarks (u,d) and of the sea quarks $\bar{u}$, $\bar{d}$ and s, $\bar{s}$ to the nucleon momentum have been extracted from semi-inclusive DIS, in which in addition to the scattered electron an emitted hadron is detected.

In this description of the nucleon, wherein the nucleon consists of quarks which interact through the exchange of gluons, the question arises how the nucleon spin is

composed. In the naive QPM the nucleon spin is the sum of the spins of the three valence quarks. Moreover, the sea-quarks and the gluons may contribute to the nucleon spin. Finally, the orbital momentum of the quarks may contribute to nucleon spin as well.

This leads to following expression for the total nucleon spin :

$$\frac{1}{2} = \frac{1}{2}\Delta\Sigma + \Delta G + L_z \,, \tag{1.1}$$

where $\Delta\Sigma$ and ΔG represent the spin contribution of quarks and gluons and L_z is the contribution from the orbital angular momentum of the quarks and gluons.

Information on the composition of the nucleon spin has been extracted from a QCD analysis of the structure function g_1. This structure function is obtained from the measured cross sections for inclusive scattering of polarized leptons off polarized nucleons over a wide range of transferred four-momentum squared Q^2 and the Bjorken scaling variable x. By integrating $g_1(x)$ over x it is concluded that only about 20 % of the nucleon spin, as predicted by the Jaffe sum rule, is accounted for by the quarks [4]. This implies a sizeable contribution of the gluons and/or the orbital angular momentum to the nucleon spin.

Thus far, theoretical studies have not yet resulted in an accurate predictions for ΔG [5, 6] as model-dependent assumptions are needed to evaluate ΔG.

The contribution of the gluons to the nucleon spin can be determined experimentally by isolating events produced by Photon-Gluon Fusion (PGF). In this process a $q\bar{q}$ pair is created that most likely fragments into two mesons. If a meson-pair with small mass (pions and kaons) is created out of a $u\bar{u}$, $d\bar{d}$ or $s\bar{s}$ pair the mesons are characterized by a large transverse momentum. If a $c\bar{c}$ pair is created the fragmentation either leads to the formation of two charmed mesons or a charmed baryon and a charmed meson of opposite charge.

Within the HERMES collaboration several investigations have been made to explore the possibilities to isolate charm production processes.

The cross section for J/Ψ electroproduction has been determined and found to be in satisfactory agreement with the existing data [7].

The cross sections for electroproduction of the $D^{*\pm}$ were extracted from the hadronic decay $D^{*+} \to D^0(\to K^-\pi^+)\pi^+$ and $D^{*-} \to \bar{D^0}(\to K^+\pi^-)\pi^-$. For this study the data taken in 1997 were used. The measured cross-sections were found to be in good agreement with perturbative QCD expectations and the world data [8, 9].

Recently an investigation of Λ_c^+ photoproduction in the decay channel $\Lambda_c^+ \to \Lambda^0\pi^+$

and $\Lambda_c^+ \to \Lambda^0 \pi^+ X$ has been performed [10]. The cross section for Λ_c^+ photo-production has been determined and found to be substantionally larger than expected for PGF alone. In addition double spin asymmeties have been measured with large statistical uncertainties.

This thesis reports on a measurement of the double-spin asymmetry of D^{*-} mesons created in a quasi-real photo production reaction, performed within the HERMES collaboration at DESY. In contrast to the D^* meson production studies mentioned above, the present work focusses on the semi-leptonic decay channel $D^{*-} \to \bar{D}^0 \pi^- \to K^+ e^- \bar{\nu}_e \pi^-$.

In chapter 2 the theory of deep-inelastic scattering (DIS) and its application to studies of the nucleon spin is briefly reviewed. Then the way to access the gluon polarization via the double-spin asymmetry is described.

In chapter 3 the results of two Monte-Carlo calculations, performed with the programs AROMA and PYTHIA, are presented and discussed. The Monte-Carlo data are used to simulate the semi-leptonic decay of charmed D^{*-} mesons. With the generated e^-, K^+ and π^- events selection criteria are developed with which the fraction of events from D^{*-} decay is enhanced with respect to the background.

Chapter 4 is devoted to a brief description of the HERMES experiment and its detectors. Special attention is given to the HERMES Particle Identification (PID) system.

In chapter 5 the analysis of data taken in the years 1999 and 2000 is described in detail, various selection criteria, mainly based on the Monte Carlo calculations, are applied to select events from D^{*-} decay. The results are presented in mass difference spectra $\Delta M = M_{D^{*-}} - M_{\bar{D}^0}$.

The ΔM spectra and the double-spin asymmetry extracted from these data are discussed in chapter 6. Surprisingly, not only events from D^{*-} decay were selected in the data analysis. A sizeable fraction of the 'background events' in the ΔM spectrum could be assigned to the decay of K^* mesons. This observation may open a new window to study the contribution of gluons to the nucleon spin.

Chapter 2

Deep-Inelastic Lepton-Nucleon Scattering

2.1 Introduction

In this chapter, the formalism for deep-inelastic lepton-nucleon scattering and in particular the creation of charmed mesons through the photon-gluon fusion process, will be briefly discussed. In section 2.2, the relevant kinematical variables needed to describe the cross section for deep inelastic scattering (DIS) of energetic electrons from nucleons are introduced. Then the formalism for DIS of unpolarized and polarized electrons from unpolarized and polarized nucleons will be discussed and applied in the quark-parton model (sections 2.3-2.5). This formalism will be extended by including the gluons, with emphasis on the production of charmed mesons (section 2.6).

2.2 Kinematical variables

The general expression for the interaction of an energetic electron with a nucleon reads as

$$l + N = l' + X,$$

where l and l' are the incident and the scattered electron, N is the target nucleon and X represents the hadrons in the final state. In this interaction an uncharged boson *i.e.* a photon or a Z^0 boson, is exchanged. At the energies provided by HERA, the reaction is dominated by the exchange of a virtual photon. In figure 2.1 this process is schematically depicted. The four-momenta of the incident and scattered electron are

indicated by $k = (\ \mathrm{E},\ \vec{k}\ )$ and $k' = (E', \vec{k'})$, respectively. The negative square of the four-momentum of the exchanged virtual photon is equal to

$$Q^2 \equiv -\mathbf{q}^2 = -(\mathbf{k} - \mathbf{k}')^2 \tag{2.1}$$

with $q = (\nu, \vec{q})$. Neglecting the electron mass this equation reduces to:

$$Q^2 \simeq 2EE'(1 - cos\theta) \overset{\text{lab}}{=} 4EE'sin^2\theta/2, \tag{2.2}$$

where θ is the scattering angle of the electron in the laboratory system.

Furthermore, the invariant mass of the photon-nucleon system is

$$W^2 \equiv (\mathbf{P} + \mathbf{q})^2. \tag{2.3}$$

For a fixed target the four-momentum of the nucleon, indicated by P, is equal to the nucleon mass M in the laboratory frame. This leads to an invariant energy W in the laboratory frame of

$$W^2 \overset{\text{Lab}}{=} M^2 + 2\,M\nu - Q^2, \tag{2.4}$$

Commonly, the DIS process is described by dimensionless scaling variables, which are defined as

$$x \equiv \frac{-q^2}{2\mathbf{P}\cdot\mathbf{q}} = \frac{Q^2}{2M\nu}, \tag{2.5}$$

where x, ranging from 0 to 1, is a measure of the inelasticity of the process (*e.g.* $x = 1$ corresponds to elastic scattering) and

$$y \equiv \frac{\mathbf{P}\cdot\mathbf{q}}{\mathbf{P}\cdot\mathbf{k}} = \frac{\nu}{E}, \tag{2.6}$$

y is the fraction of the initial lepton energy transferred by the photon to the nucleon.

When in addition to the scattered electron an emitted hadron is detected, the reaction is named semi-inclusive DIS. Two additional scaling variables are introduced to describe this process. The first one represents the fraction of the energy z acquired by the emitted hadron, which is defined as

$$z \equiv \frac{\mathbf{P}\cdot\mathbf{P}_h}{\mathbf{P}\cdot\mathbf{q}} \overset{Lab}{=} \frac{E_h}{\nu}. \tag{2.7}$$

E_h is the energy transferred to the hadrons in the final state and $\mathbf{P}_h = (E_h, \vec{p}_h)$ indicates the four-momentum of a final-state hadron. The other one is defined as

$$x_F \equiv \frac{p_\parallel}{|\,\vec{q}\,|} \simeq \frac{2p_\parallel}{W}, \tag{2.8}$$

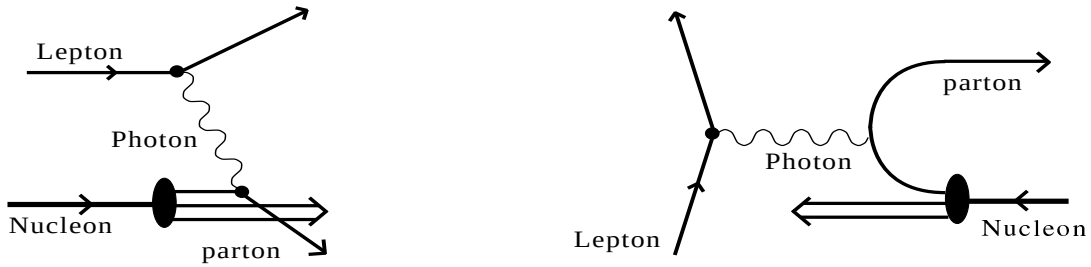

Figure 2.1: Deep-inelastic lepton-nucleon scattering in the parton model, presented in the laboratory frame and in the Breit frame.

where $p_{\parallel}$ is the longitudinal momentum component of the hadron, and distinquishes between hadrons from the interaction (so-called current fragmentation with $x_F \geq 0$), and hadrons from the target remnant ($x_F \leq 0$).

2.3 Inclusive Deep-Inelastic Scattering

Assuming one-photon exchange the cross section for DIS of a lepton from a nucleon can be expressed as the product of a lepton tensor $L_{\mu\nu}$ and a hadron tensor $M^{\mu\nu}$ [11, 12],

$$\frac{d^2\sigma}{dE'd\Omega} = \frac{\alpha^2}{Q^4}\frac{E'}{E}L_{\mu\nu}W^{\mu\nu}, \tag{2.9}$$

where Ω denotes the solid angle and α the electromagnetic coupling constant. The lepton tensor contains the product of the lepton currents. If the electron and target nucleon are unpolarized one has to average over the spins in the initial state and to sum over the spins in the final state. In this case the lepton tensor reads as

$$L_{\mu\nu} = \frac{1}{2}\Sigma\bar{u}(\mathbf{k}', \mathbf{s}')\gamma_\mu u(\mathbf{k}, \mathbf{s})\bar{u}(\mathbf{k}, \mathbf{s})\gamma_\nu u(\mathbf{k}', \mathbf{s}'), \tag{2.10}$$

in which $\mathbf{s}$ and $\mathbf{s}'$ are the spins in the initial and final states, respectively. The hadron tensor $W_{\mu\nu}$ cannot be calculated from first principles. Instead, for hadrons with spin $s = \frac{1}{2}\hbar$ this tensor is parametrized in terms of structure functions. Current conservation implies that only two structure functions are required to describe the hadron

tensor for the interaction of unpolarized leptons with unpolarized nucleons. In this case the hadron tensor can be decomposed in a spin independent symmetric part ($W^S_{\mu\nu}$) and a spin dependent anti-symmetric part ($W^A_{\mu\nu}$). The spin independent part of this tensor is given by [11, 12]

$$W^S_{\mu\nu} = W_1 \left(-g_{\mu\nu} + \frac{\mathbf{q}_\mu \mathbf{q}_\nu}{\mathbf{q}^2} \right) + W_2 \frac{1}{M^2} \left(\mathbf{P}_\mu - \frac{\mathbf{P}\cdot\mathbf{q}}{\mathbf{q}^2}\mathbf{q}_\mu \right) \left(\mathbf{P}_\nu - \frac{\mathbf{P}\cdot\mathbf{q}}{\mathbf{q}^2}\mathbf{q}_\nu \right). \qquad (2.11)$$

In this equation $g_{\mu\nu}$ denotes the metric tensor.

The structure functions W_1 and W_2 parametrize the current for unpolarized hadrons. They are functions of two invariants $\mathbf{P}.\mathbf{q}$ and $\mathbf{q}^2$, and can be rewritten as

$$F_1(x, Q^2) \equiv M W_1(\mathbf{P}.\mathbf{q}, \mathbf{q}^2), \qquad F_2(x, Q^2) \equiv \nu W_2(\mathbf{P}.\mathbf{q}, \mathbf{q}^2). \qquad (2.12)$$

With the equations (2.10), (2.11) and (2.12) the cross section for unpolarized electron scattering from unpolarized nucleons can be expressed as

$$\frac{d^2\sigma}{dE' d\Omega} = \frac{4\pi\alpha^2}{Q^4} \left[y^2 F_1(x, Q^2) + \frac{1}{x}(1 - y - \frac{Mxy}{2E}) F_2(x, Q^2) \right]. \qquad (2.13)$$

Similarly, $W^A_{\mu\nu}$ can be expressed in the structure functions $g_1(x, Q^2)$ and $g_2(x, Q^2)$. These structure functions are related to the cross-section asymmetries A_1 and A_2 as

$$A_1(x, Q^2) \equiv \frac{\sigma^T_{\frac{1}{2}} - \sigma^T_{\frac{3}{2}}}{\sigma^T_{\frac{1}{2}} + \sigma^T_{\frac{3}{2}}}, \qquad A_2(x, Q^2) \equiv \frac{\sigma^{LT}_{\frac{1}{2}}}{\frac{1}{2}(\sigma^T_{\frac{1}{2}} + \sigma^T_{\frac{3}{2}})}. \qquad (2.14)$$

The terms σ^T and σ^{LT} represent the cross sections for absorption of a transversely polarized virtual photon and for the interference of the longitudinal and transverse virtual-photon amplitudes, respectively. The asymmetry A_1 accounts for the difference in the cross sections for a reaction involving a helicity change of the nucleon, while A_2 accounts for a change of the photon helicity. The structure functions $g_1(x, Q^2)$ and $g_2(x, Q^2)$ can be accessed by measuring the cross section for DIS of longitudinal polarized electrons from longitudinally and transversely polarized target nucleons, respectively. However, usually the double-spin asymmetry is measured.

The double-spin asymmetries are defined as

$$A_\parallel \equiv \frac{\sigma^{\overrightarrow{\Leftarrow}} - \sigma^{\overrightarrow{\Rightarrow}}}{\sigma^{\overrightarrow{\Leftarrow}} + \sigma^{\overrightarrow{\Rightarrow}}}, \qquad A_\perp \equiv \frac{\sigma^{\rightarrow\Downarrow} - \sigma^{\rightarrow\Uparrow}}{\sigma^{\rightarrow\Downarrow} + \sigma^{\rightarrow\Uparrow}}, \qquad (2.15)$$

where ($\overrightarrow{\Leftarrow}$) $\overrightarrow{\Rightarrow}$ denotes the case where lepton ($\rightarrow$) and nucleon ($\Leftarrow$ or $\Rightarrow$) spins are aligned (anti) parallel.

Both asymmetries linearly depend on the photon absorption asymmetries A_1 and A_2 or - equivalently on - the structure functions g_1 and g_2. Neglecting $A_\perp$, which is small at small scattering angles, *i.e.* neglecting the contribution of g_2 to the double spin asymmetry $A_\parallel$, the relation between $A_\parallel$ and A_1 reads as

$$\frac{A_\parallel}{D(1+\eta\gamma)} \approx \frac{g_1}{F_1} \approx A_1, \tag{2.16}$$

where $D \equiv \frac{y(2-y)}{y^2+2(1-y)(1+R)}$ represents the depolarization factor. Here, R is the ratio of the cross sections for longitudinally and tranversely polarized virtual photons, *i.e.* $R \equiv \frac{\sigma_L}{\sigma_T}$. Futhermore, $\gamma^2 = \frac{4M^2x^2}{Q^2}$ and $\eta \equiv \frac{2\gamma(1-y)}{(2-y)}$ are kinematical factors.

2.4 The Quark-Parton Model

In the quark-parton model DIS is described as incoherent scattering of an electron from the point-like constituent of the nucleon. The description is based on the observation that at large Q^2 and W, the structure functions F_1 and F_2 are independent of Q^2, and can be expressed as function of the Bjorken scaling variable x [13, 14, 15].

These observations are explained within the Quark-Parton model (QPM). In this model lepton-nucleon scattering is described as incoherent elastic scattering of leptons from partons, the latter being point-like particles with spin $\frac{1}{2}\hbar$ [16, 17], which were later called quarks.

In the infinite momentum frame (Breit frame), in which the nucleon momentum is large compared to the quark masses, the partons carry a fraction x of the nucleon momentum. Hence, for the quark momentum one has $p_q = xP$. This is illustrated in figure 2.1.

In this picture of incoherent lepton-quark scattering the momentum distribution of the partons is described by a distribution function $q_f(x)$, which represents the probability of finding in the nucleon a quark with a fraction x of the nucleon momentum.

The quark density (u and d) and anti-quark density ($\bar{u}$ and $\bar{d}$) in the nucleon are normalized such that the number of the various kind of (anti)quarks corresponds to that of the constituent valence quarks in the nucleons. Hence, for the proton one has

$$\int (u(x) - \bar{u}(x))dx = 2, \qquad \int (d(x) - \bar{d}(x))dx = 1. \tag{2.17}$$

For the other quarks the integral is zero.

Including the spins of the partons the distribution $q_f(x)$ can be written as

$$q_f(x) \equiv q_f^{\overrightarrow{\leftarrow}}(x) + q_f^{\overrightarrow{\rightarrow}}(x), \qquad \Delta q_f(x) \equiv q_f^{\overrightarrow{\leftarrow}}(x) - q_f^{\overrightarrow{\rightarrow}}(x) \tag{2.18}$$

where $q_f^{\overrightarrow{\leftarrow}}(x)$ and $q_f^{\overrightarrow{\rightarrow}}(x)$ are the probabilities that the spin of the quark is anti-parallel or parallel to the nucleon spin.

Within the quark-parton model the structure functions for scattering of unpolarized leptons from unpolarized nucleons is given by

$$F_1(x) = \frac{1}{2} \sum_f e_f^2 \, q_f(x) \quad , \quad F_2(x) = x \sum_f e_f^2 \, q_f(x) \, . \tag{2.19}$$

The spin-dependent structure functions for polarized nucleons can be written as

$$g_1(x) = \frac{1}{2} \sum_f e_f^2 \, \Delta q_f(x) \quad , \quad g_2(x) = 0 \, . \tag{2.20}$$

Measurements of the structure function F_2 have revealed the limitations of the quark-parton model. The results of these measurements showed that only about 50 % of the nucleon momentum can be attributed to quarks. A comprehensive description of the dynamics of the nucleon is given by QCD. In this field theory quarks interact through the exchange of (massless) gluons with spin $s = 1\hbar$, which are believed to be responsible for the remainder of the nucleon momentum.

2.5 Semi-inclusive Deep-Inelastic Scattering

2.5.1 Cross sections in semi-inclusive DIS

More detailed information on the quarks and gluons in the nucleon may be obtained from semi-inclusive deep-inelastic scattering (SIDIS). In such experiments a hadron is detected in coincidence with the scattered electron. This process is shown schematically in figure 2.2.

After absorption of the virtual photon the quark fragments in two or more hadrons. Moreover, the remaining quarks also lead to the production of hadrons.

These two classes of hadrons can be distinguished according to their momenta. In 'current fragmentation' the struck quark is a constituent of one of the created created hadrons, whereas the 'target fragments' are related to the remnants of the nucleon. The relation between the momentum of the struck quark and the momentum of the hadron created in the fragmentation process allows one to extract information on the quark momentum and spin in the nucleon from SIDIS experiments (see section 2.5.2).

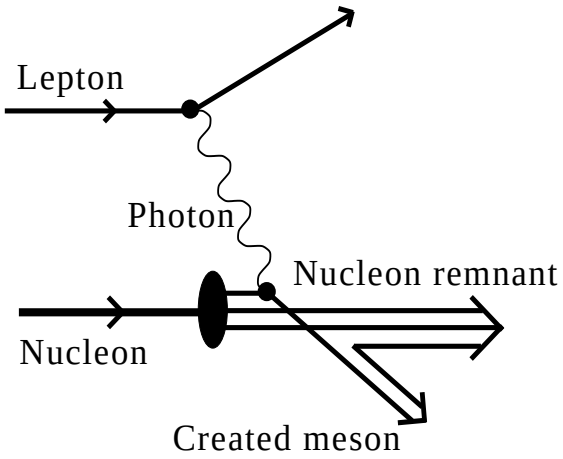

Figure 2.2: Schematic representation of semi-inclusive deep-inelastic electron-nucleon scattering.

Two Lorentz invariant scaling variables are introduced to characterize the properties of the hadrons in the final state. The first one, $z \equiv \frac{\mathbf{P}\cdot\mathbf{P}_h}{\mathbf{P}\cdot\mathbf{q}}$ is related to the energy of the hadron in the laboratory frame, *i.e.* $z = E_h/\nu$. The other one is the Feynman variable x_f, which is in the $\gamma^* + N$ center-of-mass system (γ^* is the virtual photon) given by $x_f \approx \frac{2p_\parallel}{W}$ (see Eq. 2.7 and 2.8).

The hadrons produced in the fragmentation of the struck quark typically have a large momentum in the direction of $\vec{q}$ and are characterized by $x_F \geq 0$ and $z \geq 0.2$, whereas hadrons from target fragmentation are characterized by $x_F \leq 0$.

The fragmentation process cannot be calculated within QCD because it involves long distance processes with low Q^2. Instead fragmentation functions are used to parametrize the fragmentation process. These fragmentation functions $D_f^h(z)$ express the probability that a quark of flavor f forms a hadron h with an energy that is a fraction z of the virtual-photon energy. In addition, they are normalized due to momentum conservation

$$\sum_h \int dz D_f^h(z) \,=\, n_h \qquad \sum_h \int z dz D_f^h(z) \,=\, 1. \tag{2.21}$$

The fragmentation functions for the various quark flavors strongly depend on their

masses, charges and their energy fraction z. At the energies of the electron beam provided by HERA, hadron production through fragmentation of u and d quarks and their anti-quarks is dominant.

If isospin and charge conjugation are used one can reduce the number of fragmentation functions for these quarks to two. These are

$$D^+ \equiv D_u^{\pi^+} = D_{\bar{d}}^{\pi^+} = D_d^{\pi^-} = D_{\bar{u}}^{\pi^-}, \tag{2.22}$$

$$D^- \equiv D_d^{\pi^+} = D_{\bar{u}}^{\pi^+} = D_u^{\pi^-} = D_{\bar{d}}^{\pi^-}. \tag{2.23}$$

Combining the cross section for inclusive deep-inelastic scattering in the QPM Eq. (2.13 and 2.19) and the fragmention functions given in Eq. (2.21) one obtains in lowest order QCD the following expression for the cross section for producing a hadron h in DIS:

$$\frac{d\sigma^h}{dz}(x,z,Q^2) = \sigma_{incl}(x,Q^2)\frac{\Sigma_f e^2 q_f(x,Q^2) D_f^h(z,Q^2)}{\Sigma_f e^2 q_f(x,Q^2)}. \tag{2.24}$$

2.5.2 The double-spin asymmetry in semi-inclusive DIS

The fragmention of quarks of different flavors into hadrons is assumed to be independent of the quark spin. This allows to extract from Eq. (2.24) an expression for the double-spin asymmetry in semi-inclusive DIS similar to that for semi-inclusive DIS cross-section given by Eq. (2.24). This expression is obtained by combining Eq. (2.15), (2.16) and (2.24). This gives

$$\frac{A_\parallel^h(x,Q^2)}{D} \approx \frac{\Sigma_f e_f^2 \Delta q_f(x,Q^2) \int dz D_f^h(z,Q^2)}{\Sigma_f e_f^2 q_f(x,Q^2) \int dz D_f^h(z,Q^2)}. \tag{2.25}$$

From measurements of the double-spin asymmetry in semi-inclusive DIS the contribution of the various quarks to the nucleon spin can be determined. Such measurements have been performed by the HERMES collaboration at an average Q^2 value of 2.5 GeV^2. The data were taken in the region $0.023 < x < 0.6$ and extrapolated to lower and higher values of x. From these data and the unpolarized distributions of quarks, the polarized distributions for quarks were evaluated at a common value of Q_0^2 [18]. The results of these studies are expressed in first moments in table 2.1.

From the results given in table 2.1 it follows that the contribution of the quarks to the nucleon spin is only $\Sigma = 0.442 \pm 0.026 \pm 0.078$ [18] of the total spin according to the Quark Parton Model. This observation points to large contributions from gluons

Δu	$= 0.61 \pm 0.02 \pm 0.08$	$\Delta\bar{u}$	$= 0.04 \pm 0.03 \pm 0.07$
Δd	$= -0.24 \pm 0.03 \pm 0.07$	$\Delta\bar{d}$	$= -0.01 \pm 0.03 \pm 0.05$
$\Delta s + \Delta\bar{s}$	$= 0.05 \pm 0.03 \pm 0.07$		

Table 2.1: First moments of the distributions of polarized quarks evaluated at $Q_0^2 = 2.5$ GeV.

and/or the orbital angular momentum of quarks and gluon spin to the nucleon spin. The gluon spin contribution to the nucleon spin can be determined by measuring the double-spin asymmetry of hadrons created by the Photon-Gluon Fusion (PGF) process. The next section is devoted to measurements, aimed at identifying PGF in an effort to determine the gluon polarization.

2.6 Charmed Quarks Created in Photon-Gluon Fusion

Charmed hadrons created in PGF may be a good probe to study the contribution of the gluon spin to the nucleon spin. Due to their relatively large mass the density of charmed (anti) quarks in the nucleon is negligible. Hence, the probability that charmed hadrons are produced in DIS is very small. Instead, the main production mechanism of these hadrons in lepton-nucleon scattering is given by photon-gluon fusion. Studies of the double-spin asymmetry of charmed hadron production are expected to provide information on the polarization of gluons in the nucleon. The cross section for this process is largest at small values of Q^2. This implies that the electron is scattered over a small angle and is generally not detected.

Figure 2.3a shows the leading-order process for the production of a $c\bar{c}$ pair in photon-gluon fusion. Next-to-leading order contributions involve additional gluon-exchange, gluon-radiation from the quark that has emitted the gluon or gluon radiation from the quark followed by PGF (Figure 2.3b-2.3e). The dominant next-to-leading order process is gluon radiation.

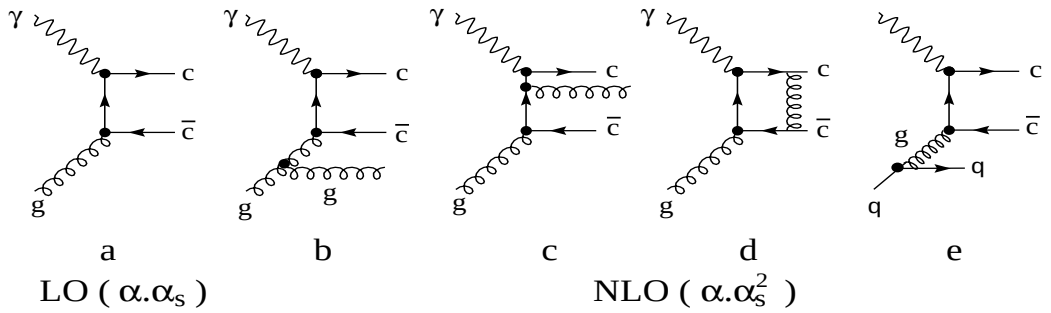

Figure 2.3: The leading order (a) and next-to-leading order(b-e) processes for the $c\bar{c}$ pair production in photon-gluon fusion.

2.6.1 Double-spin asymmetry in photon-gluon fusion

The cross section for the process $\gamma g \rightarrow c\bar{c}$ can be factorized in a convolution of the gluon distribution and the hard photon-gluon fusion process,

$$\sigma^{\gamma N \rightarrow c\bar{c}X}(\nu) = \int_{4m_c^2}^{2M\nu} d\hat{s}\, \hat{\sigma}^{\gamma g \rightarrow c\bar{c}}(\hat{s})\, g(x_g, \hat{s}). \tag{2.26}$$

Similarly, the cross-section difference $\Delta\sigma$ for photon-gluon fusion with parallel and anti-parallel spin orientations reads

$$\Delta\sigma^{\gamma N \rightarrow c\bar{c}X}(\nu) = \int_{4m_c^2}^{2M\nu} d\hat{s}\, \Delta\hat{\sigma}^{\gamma g \rightarrow c\bar{c}}(\hat{s})\, \Delta g(x_g, \hat{s}). \tag{2.27}$$

In these expressions $\hat{s} = s(\gamma g)$ is the square of the center of mass energy of the photon-gluon system, $g(x_g, \hat{s})$ is the gluon structure function and x_g is the fraction of the nucleon momentum carried by the gluon,

$$x_g = \frac{s(\gamma g)}{s(\gamma N)} = \frac{\hat{s}}{2M\nu}. \tag{2.28}$$

The spin-dependent partonic cross section for creation of heavy quarks in photon-gluon fusion, expressed in the Mandelstam variables and integrated over the azimuthal angle is given by [19]

$$d\,\Delta\hat{\sigma}_0 \;=\; \frac{\alpha_s}{4\pi}\frac{1}{(\hat{s}\;+\;Q^2)^2}\frac{1\;-\;(1\;-\;y)^2}{2}[\frac{Q^2\;-\;\hat{s}}{\hat{s}\;+\;Q^2}\;+\;\frac{2m_q^2(\hat{s}\;+\;Q^2)}{\tilde{u}\tilde{t}}]\frac{\tilde{u}^2\;+\;\tilde{t}^2}{\tilde{u}\tilde{t}}, \qquad (2.29)$$

where $\tilde{t} = {m^2}_Q - \hat{t}$ and $\tilde{u} = {m^2}_Q - \hat{u}$ and m_Q is the mass of the heavy quark.

The sign of $\Delta\sigma$ is determined by the two terms within brackets. For $Q^2 \approx 0$ the sum of both terms is positive when a $c\bar{c}$-pair is created in PGF and negative for a massless quark-antiquark pair. This implies, at the partonic level, a positive value for the double-spin asymmetry for a PGF if a $c\bar{c}$ pair is created [19].

The double-spin asymmetry for a PGF reaction in which a $c\bar{c}$ pair is created is expressed as

$$A_{\parallel}^{c\bar{c}} \;=\; \frac{\Delta\sigma^{\gamma N\rightarrow c\bar{c}}}{\sigma^{\gamma N\rightarrow c\bar{c}}} \approx \frac{\Delta\sigma^{\gamma g\rightarrow c\bar{c}}}{\sigma^{\gamma g\rightarrow c\bar{c}}}\frac{\Delta G}{G} \equiv \hat{a}_{PGF}\frac{\Delta G}{G}. \qquad (2.30)$$

In this expression the averaging over the range in $\hat{s}$ probed in the experiment is replaced by taking the central value for $\sqrt{\hat{s}}$, which is reasonable since the range in $\hat{s}$ is small. A lower value of about 4 GeV for $\hat{s}$ is determined by the threshold energy E_{thresh} for the production of charmed hadrons while the maximum value of $\hat{s}$ is set by the available energy in the electron-nucleon center-of-mass system, which amounts for 27 GeV electrons to

$$\sqrt{s} \;\stackrel{Lab}{=}\; \sqrt{E_e^2\;+\;M^2\;+\;2ME_e} \;\approx\; 7.3\,\mathrm{GeV}, \qquad (2.31)$$

where E_e and M are the electron energy and the nucleon mass, respectively.

Hence, effectively the asymmetry is evaluated at an average $\sqrt{\hat{s}}$ of about 5.5 GeV.

2.6.2 Formation of charmed hadrons near threshold

The maximum energy of about 7 GeV available in the electron-nucleon center-of-mass system is close to the threshold energy for production of charmed mesons, meson-pairs and hadron-meson pairs that can be formed in the fragmentation of a $c\bar{c}$ pair (see table 2.2). This implies that the production rate of charmed hadrons in the HERMES experiment is expected to be small compared to the production rate of pions and strange mesons.

At larger values of $\sqrt{s}$ charmed mesons are also created in the decay of B-mesons and produced in other processes, *e.g.* gluon-gluon fusion. At an electron energy $E_e =$ 27 GeV the contribution of these processes is negligible.

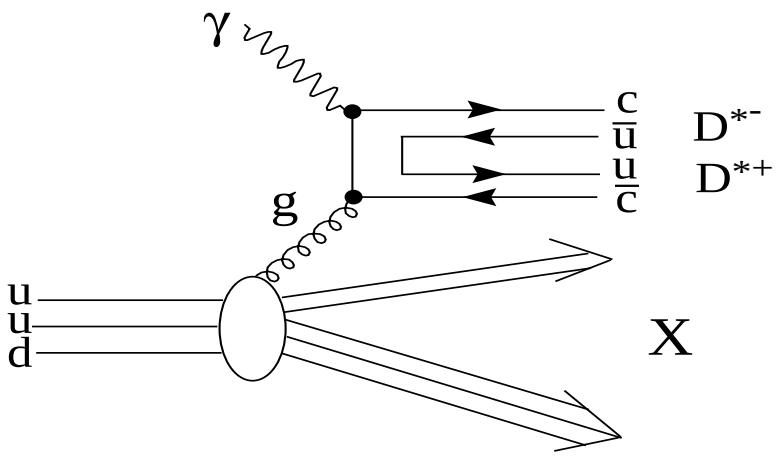

Figure 2.4: Production of D^{*-} and D^{*+}- mesons in PGF.

Particles	Quark Content	Mass MeV/c^2	Full Width MeV	Mean Lifetime 10^{-15}s
$D^{*0}, \bar{D}^{*0}$	$c\bar{u}$ $\bar{c}u$	2006.7 ± 0.5	< 2.1	
$D^{*+}, \bar{D}^{*-}$	$c\bar{d}$ $\bar{c}d$	2010.0 ± 0.5	< 0.131	
$D_s^{*+}, \bar{D}_s^{*-}$	$c\bar{s}$ $\bar{c}s$	2112.4 ± 0.7	< 1.9	
$D^0, \bar{D}^0$	$c\bar{u}$ $\bar{c}u$	1864.6 ± 0.5		411.7 ± 2.7
D^+, D^-	$c\bar{d}$ $\bar{c}d$	1869.3 ± 0.5		1051 ± 13
D_s^+, D_s^-	$c\bar{s}$ $\bar{c}s$	1968.5 ± 0.6		490 ± 9
η_c	$c\bar{c}$	2979.7 ± 15	$16.0^{3.6}_{3.2}$	
J/ψ	$c\bar{c}$	3096.8 ± 0.04	0.087 ± 0.005	
Λ_c^+, $\bar{\Lambda}_c^+$	udc $\bar{u}\bar{d}\bar{c}$	2284 ± 0.6		200 ± 6

Table 2.2: Properties of the charmed hadrons which can be produced at center-of-mass energies available at the HERMES experiment.

Mesons created in the fragmentation of a $c\bar{c}$ pair can be distinguished into two categories, depending on their content of (anti)charmed quarks. They either contain a $c\bar{c}$ pair (hidden charm) or a c-quark (or $\bar{c}$-quark) in combination with a u, d, s-quark or antiquark (open charm). The first category consists of the η_c and J/ψ mesons, and the second one of D, D^* and D_s (anti)mesons (table 2.2). Open charm hadron production probabilities for photon-gluon fusion as a function of lepton beam energy are illustrated on Fig. 2.5.

The fragmentation of charmed-quarks into charmed-hadrons can be described phenomenologically by the 'Peterson fragmentation function', which can be expressed as [20]

$$D_c^H(z) \;=\; \frac{N}{z[1 \,-\, \frac{1}{z} \,-\, \frac{\epsilon}{(1-z)}]^2}. \tag{2.32}$$

where z is the energy fraction of hadron H with respect to the charmed quark, N is a normalization factor such that $\sum_h \int dz D_c^H(z) = 1$. The parameter ϵ variates in the range of 0.025- 0.075 and has to be extracted from fits to the data.

For charmed hadrons produced in the fragmentation of c and $\bar{c}$ quarks, which in turn are created in PGF, the double-spin asymmetry is equal to that given by Eq. (2.30). Hence, the double-spin asymmetry measured for charmed mesons contains information on $\frac{\Delta G}{G}$. However, the process fraction which is given by the fraction of all events produced by PGF over all events leading to the same final states, is not unity for charmed hadrons. As will be discussed in the next section, charmed hadrons, and in particular charmed mesons in combination with charmed baryons, also produced in other processes. As mentioned before, the sign of $A_{\parallel}^{c\bar{c}}$ is determined by the parton asymmetry $\hat{a}_{PGF}$, which is expected to be positive for charmed quarks [21].

2.6.3 Additional production mechanisms for charmed hadrons

In the previous subsections it was argued that the contributions of intrinsic charm ($c\bar{c}$) pairs and of the decay of B-mesons created in the fragmentation of ($b\bar{b}$) pairs can be discarded. However, additional contributions to charmed hadrons are due to processes in which the charmed quark is contained in the target remnant and in addition an anti-charmed meson is produced. For example, this occurs in the production of a charmed meson in combination with a Λ_C baryons, which contains two valence quarks from the target-remnant and a c-quark. In a PGF reaction on a proton the following processes may occur

$$\gamma p \rightarrow \Lambda_C^+ \,+\, D^- \,+\, \pi^+ \quad \text{and} \quad \gamma p \rightarrow \Lambda_C^+ \,+\, D^{*-} \,+\, \pi^+.$$

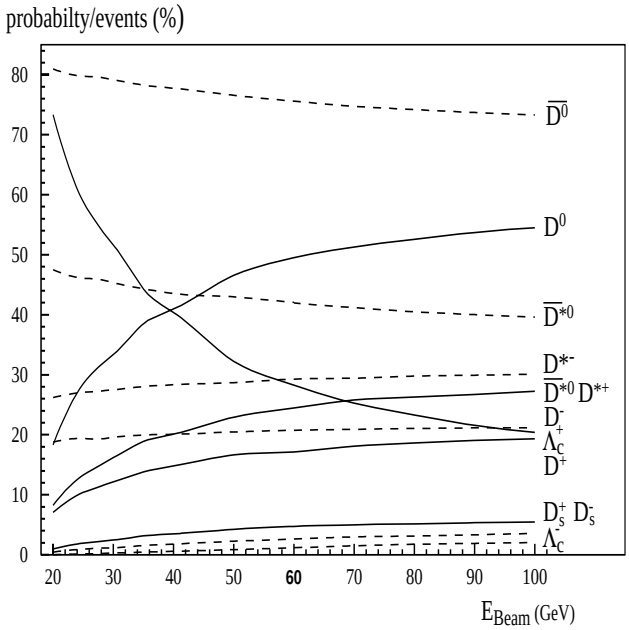

Figure 2.5: Open charm production probabilities for photon-gluon fusion in lepton proton scattering as a function of lepton beam energy. Results are obtained from the AROMA (see Chapter 3) simulation using the 'Peterson fragmentation function' [8].

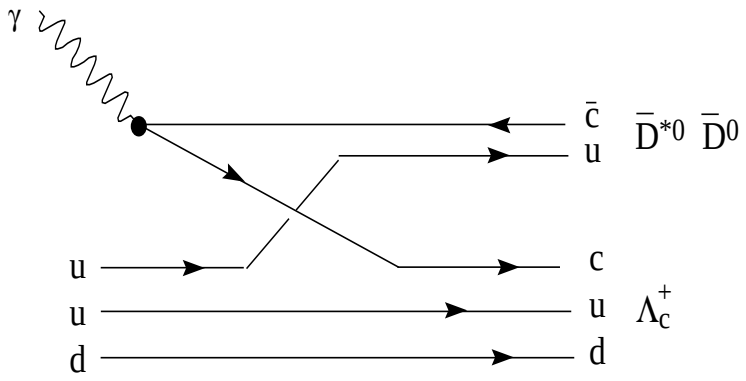

Figure 2.6: Quark-exchange process which contributes to the production of Λ_C^+, $\bar{D}^0$ and $\bar{D}^{*0}$.

In these processes the final state contains three hadrons. However, when a $\bar{D}^0$ or $\bar{D}^{*0}$ is created in association [22] with a Λ_C^+ baryon via quark-exchange the final state contains only two hadrons, see Fig. 2.6,

$$\gamma p \rightarrow \Lambda_C^+ + \bar{D}^0 \qquad \text{and} \quad \gamma p \rightarrow \Lambda_C^+ + \bar{D}^{*0}.$$

The latter process is particularly important near threshold. This follows from the Monte Carlo calculations with AROMA, performed by Volk [8].

2.6.4 Decay of the D^{*-} meson

In table 2.3 the main decay-modes of the D^{*-} and the $\bar{D}^0$ mesons are given. The main decay channel of the D^{*-} is $D^{*-} \rightarrow \bar{D}^0\pi^-$, which accounts for 68% of the total decay. The $\bar{D}^0$ decay has several branches, including two or three particles in the final state. Within the HERMES collaboration several of these decay channels have been studied. The cross section $\sigma^{ep} \rightarrow D^{*-}$ on a ^{1}H-target has been measured Brons [9], Volk [8] and Scarlett [23]. This cross-section was extracted from the number events measured for the hadronic decay $D^{*-} \rightarrow \bar{D}^0\pi^- \rightarrow K^+\pi^-\pi^-$, selected in the reconstructed mass difference spectrum $\Delta M = M(D^{*-}) - M(\bar{D}^0)$. This mass difference spectrum is shown in fig. 2.7. The highlighted region of ΔM_0 indicates the area where the signal $D^{*-} \rightarrow K^+\pi^-\pi^-$ is expected. Futhermore, a study of the hadronic decay $\bar{D}^0 \rightarrow K^+\pi^-\pi^0$ is in progress.

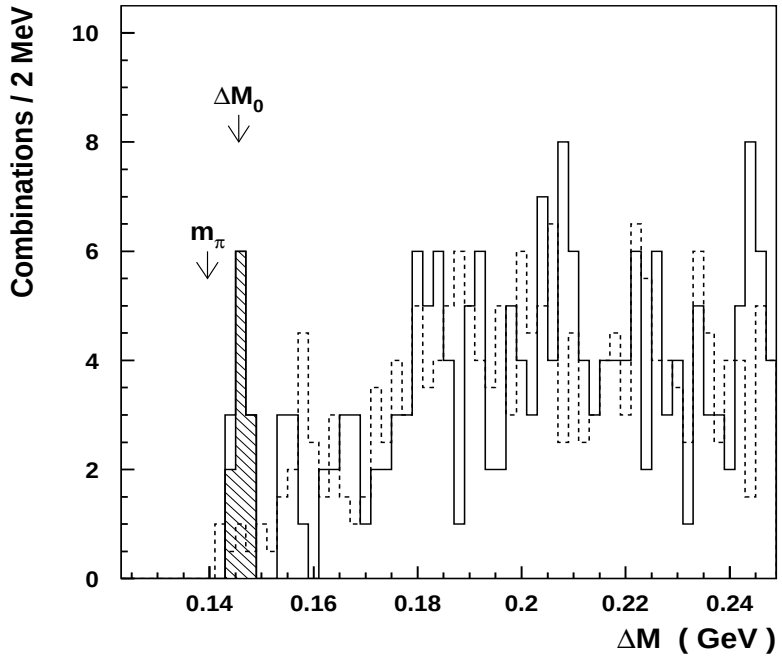

Figure 2.7: Mass-difference spectra for the hadronic decay of D^{*-} mesons obtained for the HERMES 1997 data. The solid histogram represents candidates for D^{*-} decay, and the dashed histogram indicates background sample.

It is evident that number of D^* mesons observed at HERMES using 1997 data is small. It is the objective of the present work to explore the prospects of extracting information on $\Delta G/G$ using the semi-leptonic decay channel ($D^{*-} \to \bar{D}^0\pi^- \to \pi^- K^+ e^- \bar{\nu}_e$) using the all data collected by HERMES in the years 1999-2000.

D^{*-} decay	fraction (%)		hadronic $\bar{D}^0$ decay	fraction (%)
$D^{*-} \Rightarrow \bar{D}^0\pi^-$	68.3 ± 1.4	$\Longrightarrow$	$\bar{D}^0 \Rightarrow K^+\pi^-$	3.85 ± 0.09
$D^-\pi^0$	30.7 ± 2.5		$K^0\pi^0$	2.12 ± 0.2
			$K^0\pi^+\pi^-$	5.4 ± 0.4
			$K^+\pi^-\pi^0$	13.9 ± 0.9
			$K^-\pi^+\pi^+\pi^-$	7.6 ± 0.4
			semi-leptonic decay	
			$K^+e^-\bar{\nu}_e$	3.6 ± 0.2
			$K^+\mu^-\bar{\nu}_\mu$	3.2 ± 0.2

Table 2.3: Selected decay-channels for the D^{*-} and $\bar{D}^0$ mesons.

Chapter 3

Monte Carlo Simulations

3.1 Introduction

In the previous chapter the production of charmed hadrons with real and quasi-real photons in the energy domain covered by the HERMES experiment was discussed. Experimental studies on the hadronic decay of $D^{*\pm}$ and Λ_C^+ particles at HERMES have shown that the cross sections for creating these hadrons with 27 GeV electrons are small [7, 8, 10]. Furthermore, these studies showed that the background in the reconstructed invariant-mass spectra and mass-difference spectra (ΔM) was relatively large. This background depends on the decay-mode of the hadrons. Hence, the ratio between the contributions of $D^{*\pm}$ decay and the background to the invariant mass spectra, is not necessarily the same for the semi-leptonic and hadronic decay. Therefore, dedicated Monte Carlo simulations for the semi-leptonic decay of the D^{*-} are needed to determine the fractions of the events in the invariant-mass and ΔM spectra stemming from the decay of charmed particles and from other processes.

Such calculations were performed with the AROMA [24] and PYTHIA6 [25] programs. With AROMA the production and semi-leptonic decay of $D^{*\pm}$ mesons were simulated. These particles were also generated with PYTHIA6. However, in the later case PFG accounts only for a small fraction of the generated events. Therefore, PYTHIA was mainly used to study the various processes contributing to the background in the invariant-mass spectra. Using the combined results of these Monte Carlo simulations, selection criteria were developed to optimize the fraction of the events from D^{*-} production in the ΔM spectra. These criteria were used in the data analysis.

In section 3.2 a brief description of the programs AROMA and PYTHIA is given. Then, the results of the calculations performed with both programs are presented and discussed in section 3.3.

3.2 The programs AROMA and PYTHIA

The program AROMA [24, 26, 27] simulates the production of heavy quarks, *i.e.* quarks with mass ≥ 1 GeV, in lepton-nucleon scattering through the boson-gluon fusion process. At the partonic level, the interactions are based on the electroweak cross-sections given by the standard model. Arbitrary polarizations and different parametrizations of parton densities can be used. At the moderate electron energies provided by HERA only photon-gluon fusion contributes to the cross section for the creation of a ($c\bar{c}$) pair. Hadronization of the partons is simulated using the LUND string model. Generally, the symmetric Lund fragmentation is used, and the creation of charmed hadrons is usually calculated with the phenomenological Peterson fragmentation function.

In recent Monte Carlo studies of Λ_C^+ and D^* production in the energy domain covered by the HERMES experiment, performed with the program PYTHIA, no significant dependence of the momentum distributions on the fragmentation functions was observed [8, 10]. The AROMA calculations for the semi-leptonic decay of the D^{*-} were performed with the phenomenological Peterson fragmentation function. No other fragmentation functions, *e.g.* the symmetric Lund fragmentation function, were considered because of the conclusions obtained in Refs. [8] and [10].

Tracks of the simulated events were generated in a model of the HERMES detector, using the HMC program in the version with the set-up of the year 2000. Subsequently, the tracks of the relevant particles were reconstructed with the HRC program. The background in the invariant mass and ΔM spectra due to other processes was studied using Monte Carlo data generated with the program PYTHIA6 [25, 28].

3.3 Monte Carlo Simulations

3.3.1 Analysis of Monte Carlo data calculated with AROMA

To simulate the invariant mass M and ΔM distributions for the semi-leptonic decay of the D^{*-} meson within the phase-space covered by the HERMES detector, 10.000 events were generated with the AROMA program. The process studied is $D^{*-} \rightarrow \bar{D}^0\pi^- \rightarrow K^+e^-\bar{\nu}_e\pi^-$ in which $\bar{\nu}_e$ goes unobserved. Only events with one π^-, one K^+ and one e^- within the acceptance of the HERMES detector were analyzed. Furthermore, the following constraints were applied to the Monte Carlo data

- The invariant mass of the two particle K^+e^- system is in the range 0.6-2.1 GeV.

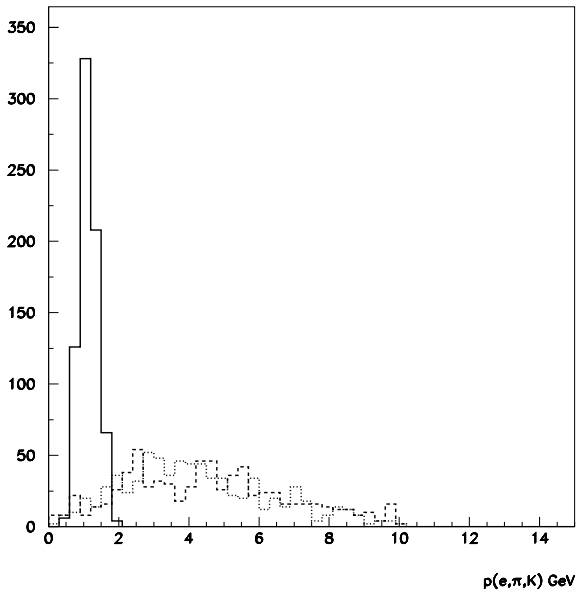

Figure 3.1: Calculated momentum distributions of charged particles created in the semi-leptonic decay of the D^{*-} meson with momenta within the acceptance of the HERMES detector. Dotted histogram: e^-, dashed histogram: K^+ and solid histogram: π^-.

- The invariant mass of the three particle system $\pi^- K^+ e^-$ is in the range 0.5-2.5 GeV.
- The momenta of the three particles $\pi^- K^+ e^-$ were required to be in the HERMES acceptance.

For the selected particles, tracks in the HERMES detector were reconstructed with the code HRC (HERMES Reconstruction Code) [29].

Figure 3.1 shows the momentum distributions for the reconstructed particles. The dotted, dashed and solid histograms represent the distributions for the electrons, kaons and pions, respectively. The small range in the momentum distribution of the π^- is due to the small mass difference between the D^{*-} meson and the sum of its decay products $\bar{\mathrm{D}}^0$ and π^-. This results into a pion momentum in the rest-frame of the D^{*-} of 41 MeV/c only.

In the further analysis only pions with momenta less than 2 GeV/c are taken into account. Furthermore, the main trigger of the HERMES detector requires a minimum energy deposition of 1.5 GeV in the Electromagnetic Calorimeter. Hence, two cuts

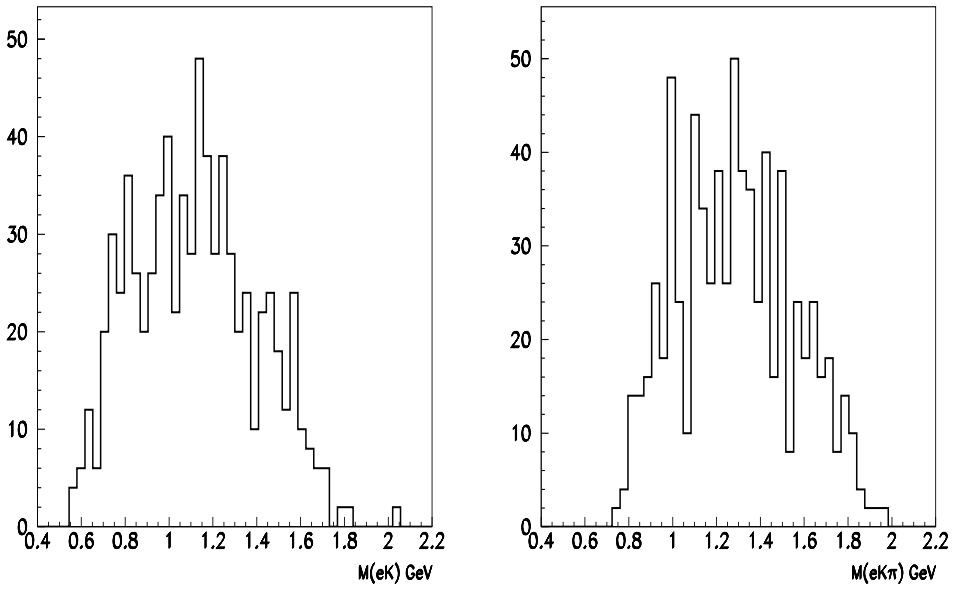

Figure 3.2: Reconstructed invariant mass spectra for decay products of the D^{*-} meson calculated with AROMA. Left - M(K^+e^-) , right M($\pi^-K^+e^-$).

were applied on the simulated data:

$p_{\pi^-} < 2.0$ GeV and $p_{e^-} > 1.5$ GeV and $p_{K^+} > 2.0$ GeV.

In figure 3.2 the invariant masses corresponding to the K^+e^- and $\pi^-K^+e^-$ systems are shown.

They account for the partially reconstructed masses of the $\bar{D}^0$ and the D^{*-} mesons, respectively. The broad distributions reflect the large momenta of the non-observed ν_e. Since the effect of the missing neutrino momentum is comparable in both distributions the width of the mass-difference distribution $\Delta M = M_{\pi^-K^+e^-} - M_{K^+e^-}$, shown in figure 3.3 (left histogram), is much smaller. Therefore, this distribution is more suited to identify events from the semi-leptonic decay of the D^{*-} meson and will be used in the data analysis. Figure. 3.3 (right histogram) shows the ΔM spectrum for events in which the pion is not emitted in the decay of the D^{*-}. The ΔM distribution for these events (which also stem from the decay of charmed hadrons) is much wider.

3.3.2 Analysis of Monte Carlo data calculated with PYTHIA

In the analysis of the Monte Carlo data generated with the program PYTHIA6, data files provided by Bailey and Makins were used [30]. To reduce the number of generated

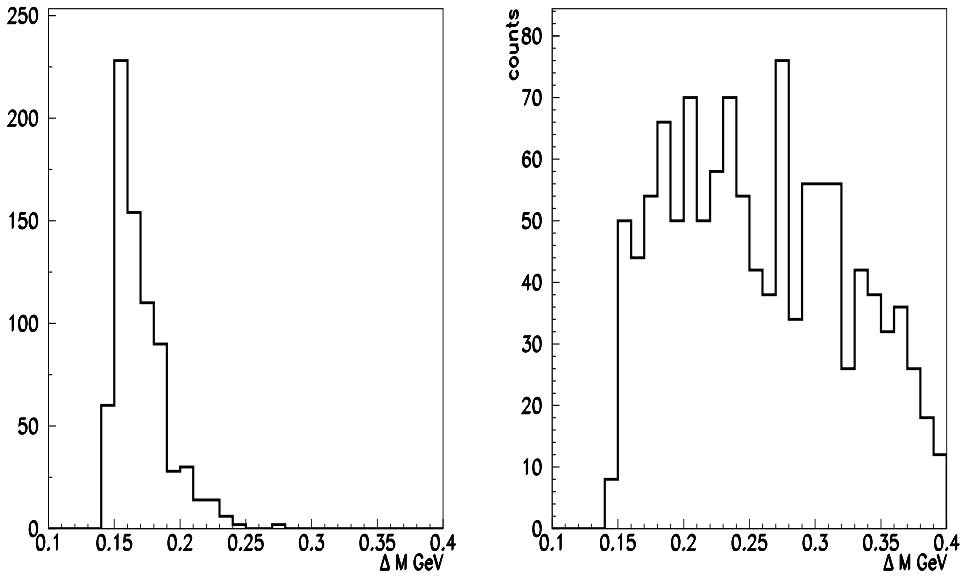

Figure 3.3: Mass difference $\Delta M = M(\pi^- K^+ e^-) - M(K^+ e^-)$ calculated with AROMA. The pion is emitted in the decay of the D^{*-} meson (left histogram).The spectrum for the case in which the pion is not emitted in the decay of the D^{*-} meson, but as a result of the fragmentation of some other meson is shown in the right histogram.

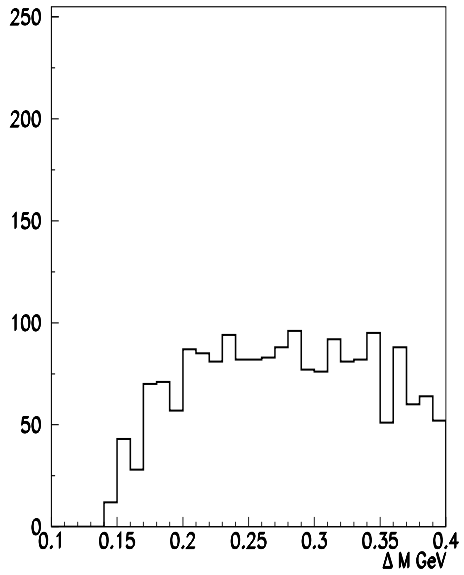

Figure 3.4: ΔM spectrum extracted from PYTHIA.

data, an event selector was employed in these calculations. Only events meeting the following requirements were accepted and stored in the output files.

- Three particles, one electron, one kaon and one pion were required.
- The invariant mass difference $M_{Ke\pi} - M_{Ke} \leq 0.5$ GeV.
- The energy of the pion is in the range 0.2 GeV $\leq E_\pi \leq$ 2.2 GeV.

Figure 3.4 shows the ΔM spectrum extracted from the PYTHIA simulation. No indication for the contribution from the semi-leptonic decay of D^{*-} mesons is visible in this spectrum. To obtain a signature for events from the decay of D^{*-} mesons the background has to be reduced. This can be achieved by reducing the physics phase space of the decay particles such that the number of 'background events' is strongly suppressed relative to the events from D^{*-} decay. In the next section the strategy, leading to a reduction of the background with a minimum loss of events from D^{*-} decay, is discussed.

3.3.3 Strategy in the analysis of the Monte Carlo data

The MC data generated with AROMA and PYTHIA were used to define a number of criteria with which events from D^{*-} decay are enhanced in the ΔM spectrum with

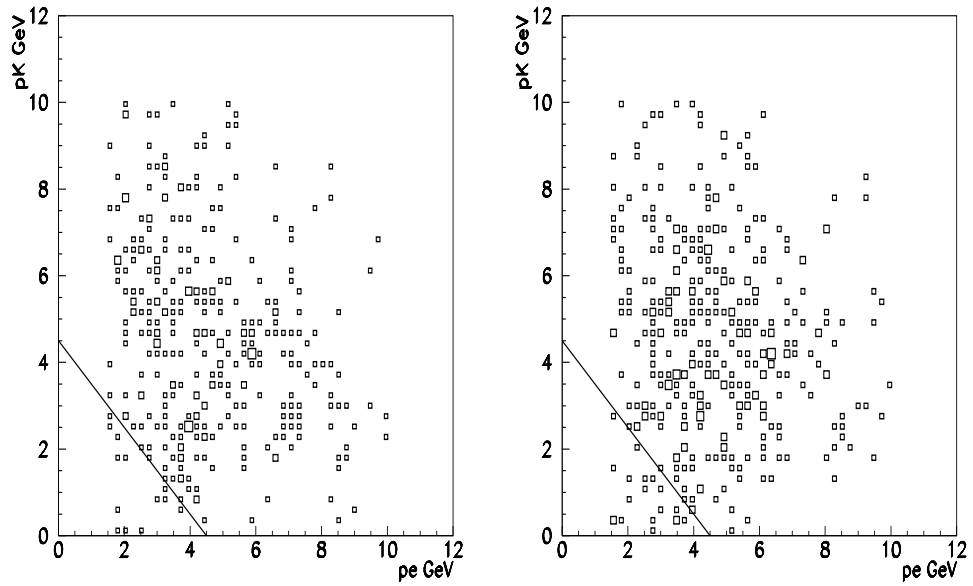

Figure 3.5: The p_{K^+} versus p_{e^-} momentum for semileptonic decay products in AROMA. The pion is emitted in the D^{*-} decay (left histogram). The pion is not emitted in the D^{*-} decay (right histogram).

respect to those from other processes. These criteria are based on some characteristic features of the phase space for the $D^{*-} \rightarrow \pi^- + \bar{D}^0 \rightarrow \pi^- + e^- + K^+$ decay. This phase space was investigated using the results of the simulations peformed with AROMA. Subsequently, the effect of the selected criteria on the 'background' was determined using the PYTHIA data. Firstly, the relation between the electron and kaon momenta was studied. If both particles are emitted in the decay of the $\bar{\mathrm{D}}^0$ meson, these momenta are correlated, as is shown in figure 3.5 (left histogram). This correlation is limited due to the emission of a (non observed) third particle in this decay.

In figure 3.5 (right histogram) the same distribution is displayed for events in which the pion is not emitted in the decay of the D^{*-} meson, but from a $\bar{\mathrm{D}}^0$ or another charmed hadron. No significant differences are visible between both distributions. Taking the sum of the electron and kaon momenta $p_e + p_K \geq 4.5$ GeV/c, in addition to the electron and pion momenta cuts, 85% of the events in which the pion is emitted in the D^{*-} decay is accepted. This fraction is 50% for the events for which the pion is not emitted in the decay of the D^{*-}.

Next, the emission angles of the electron and kaon relative to pion momentum are examined. It is expected that these angles are small for events from the decay

$D^{*-} \rightarrow \pi^- + \bar{\mathrm{D}}^0 \rightarrow \pi^- + e^- + K^+$. Due to the small mass difference between both charmed mesons ($\Delta M = M_{D^{*-}} - M_{D^0} = 0.146\,\mathrm{GeV/c^2}$) , the pion and $\bar{D}^0$ acquire almost no momentum in the D^{*-}-rest frame. Hence, the transverse momentum of both particles with respect to the D^{*-} and $\bar{\mathrm{D}}^0$ momenta is small. This implies that $\theta_{p_{e^-}p_{\pi^-}}$ and $\theta_{p_{K^+}p_{\pi^-}}$ are effectively the angles of the electron and kaon momenta with respect to the $\bar{D}^0$-momentum. Furthermore, the transverse momenta acquired by the K^+ and e^- are small relative to the $\bar{D}^0$-momentum. Hence, the average emission-angles of both particles with respect to the $\bar{D}^0$ and with respect to the π^- are small. This is reflected by the results of the calculations performed with AROMA, which are displayed in figure 3.6(left histogram). The curves in this figure are in accordance with the relation: $(1 - \cos(\theta_{p_{K^+}p_{\pi^-}})) \times (1 - \cos(\theta_{p_{e^-}p_{\pi^-}})) < (0.016)^2/2$

Only 2.2% of the events of figure 3.6 (left histogram) is beyond the domain limited by the following conditions:

$$1 - \cos(\theta_{p_{K^+}p_{\pi^-}}) > 0.03$$
$$1 - \cos(\theta_{p_{e^-}p_{\pi^-}}) > 0.03$$
$$(1 - \cos(\theta_{p_{K^+}p_{\pi^-}})) \times (1 - \cos(\theta_{p_{e^-}p_{\pi^-}})) < (0.016)^2/2)$$

In figure 3.6 (right) the same distribution is shown for events in which the pion is not emitted in the decay of the D^{*-} meson, but originated from the decay of other particles produced in the AROMA simulation. Of these events 54% is beyond the selected domain for the emission angles.

Finally, correlations in the distribution of the reconstructed $\bar{\mathrm{D}}^0$ mass versus the pion momentum were investigated. Figure 3.7 shows these distributions for events in which the pion is emitted in the decay of the D^{*-}, and those stemming from other processes, respectively. The horizontal and vertical lines mark the selected domain. From the events in which the pion is emitted in the D^{*-} decay 84 % is accepted.

The selection criteria discussed above have also been applied to the data extracted from the simulations with PYTHIA. The results are shown in the figures 3.8 and 3.9. These figures clearly indicate that the background is largely suppressed by setting constraints on the various variables discussed above.

3.3.4 Mass-difference spectra

The effect of the various cuts on the mass-difference spectra ΔM is shown in the figures 3.10, 3.11 and 3.12 for the calculations performed with AROMA and PYTHIA, respectively. It is clear from these figures that the shape of the spectra calculated with

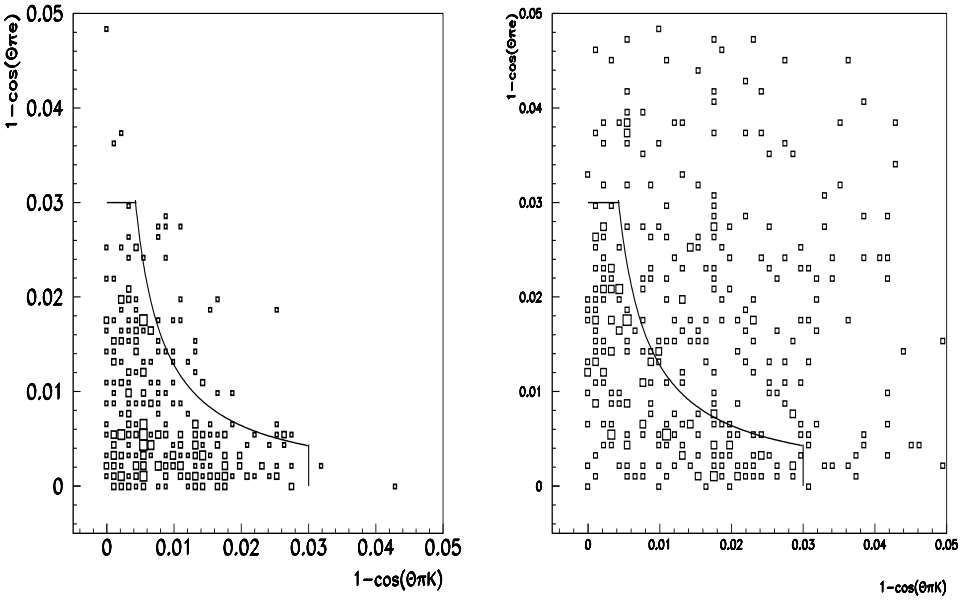

Figure 3.6: Angular distribution of decay products in semi-leptonic decay of D^{*-} meson as evaluated with AROMA. The pion is emitted in the D^{*-} decay (left histogram). The pion is not emitted in the D^{*-} decay (right histogram).

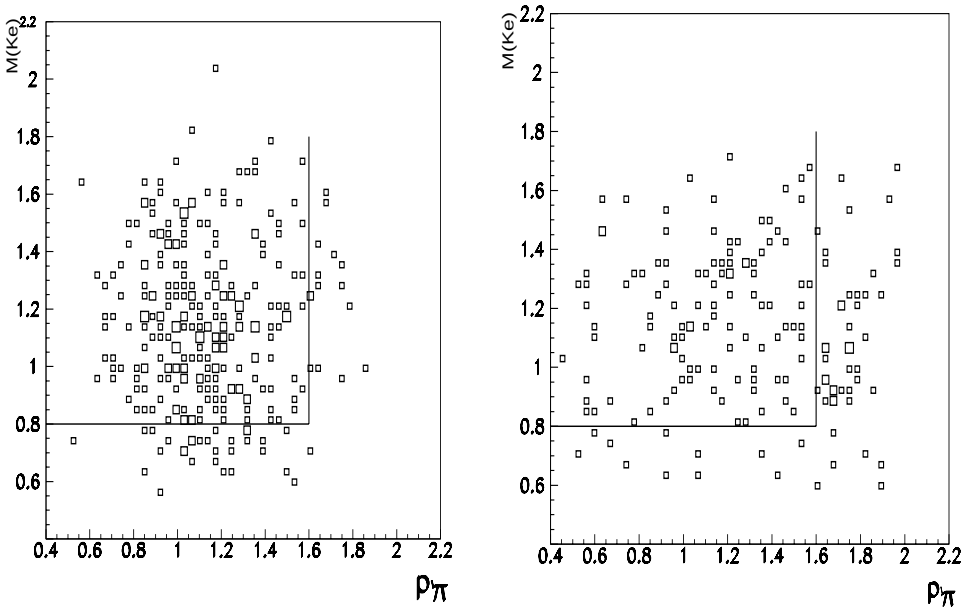

Figure 3.7: Reconstructed invariant mass of the (K^+e^-) system versus the momentum of the pion p_{π^-} obtained with AROMA. The pion is emitted in the D^{*-} decay (left histogram), while the pion is not emitted in the D^{*-} decay (right histogram).

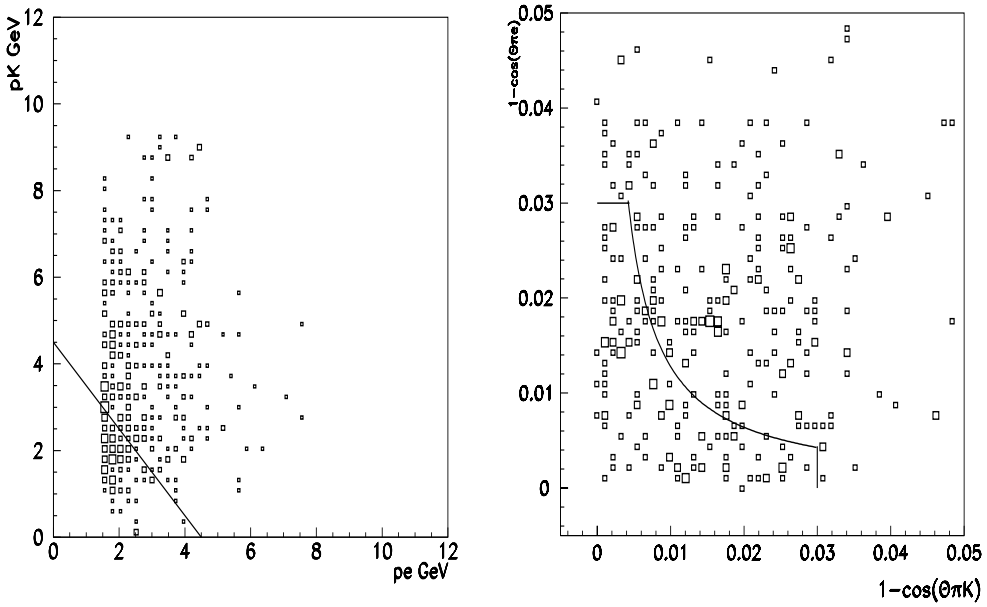

Figure 3.8: p_{K^+} versus p_{e^-} for background decay products in PYTHIA (left histogram). Angular distributions for 'background' events calculated with PYTHIA (right histogram).

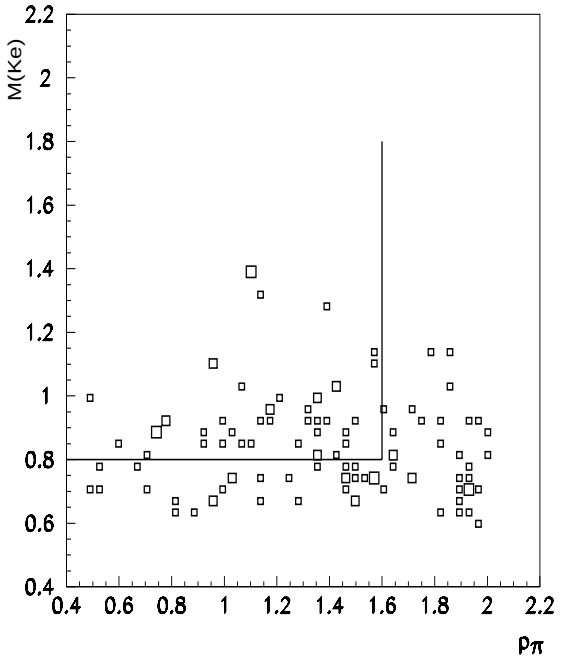

Figure 3.9: Reconstructed invariant mass of the (K^+e^-) system versus p_{π^-} calculated with PYTHIA for 'background events'.

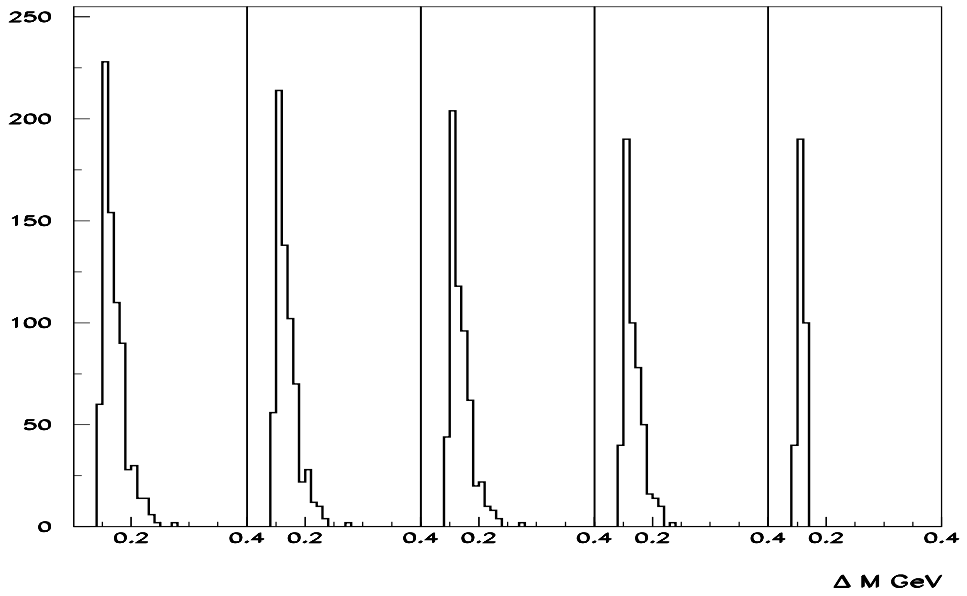

Figure 3.10: Mass-difference spectra for decay products of the D^{*-} calculated in AROMA after various cuts on the data.

AROMA for events in which the pion is emitted by the D^{*-} are not strongly affected, and that the yield is not strongly reduced by the respective cuts applied to the Monte Carlo data. In the contrary, the backgound simulated with PYTHIA is reduced by about a factor 3000.

This result is presented in a more quantitative way in table 3.1. In this table the fractions of the events, being left after the various cuts, are given for both calculations. Table 3.2 shows the same numbers after normalization to the number of events extracted from the HMC code without any further selection. This table directly indicates that from the events in which the pion is emitted in the decay of D^{*-} about 70% is left over after all cuts, and that this fraction is only 15% and 2% for the other processes respectively. The respective cuts are:

A. $p_{\pi^-} < 2$ GeV, $p_{e^-} > 1.5$ GeV, $p_{K^+} \geq 2$ GeV, $p_{e^-} + p_{K^+} \geq 4.5$ GeV
B. $1 - \cos(\theta_{p_{K^+}p_{\pi^-}}) < 0.03$, $1 - \cos(\theta_{p_{e^-}p_{\pi^-}}) < 0.03$ and
$(1 - \cos(\theta_{p_{K^+}p_{\pi^-}})) \times (1 - \cos(\theta_{p_{e^-}p_{\pi^-}}) < (0.016)^2/2)$
C. $M(K^+e^-) > 0.8$ GeV, $p_{\pi^-} < 1.6$ GeV

because the RICH detector is able to identify only kaons within momentum range

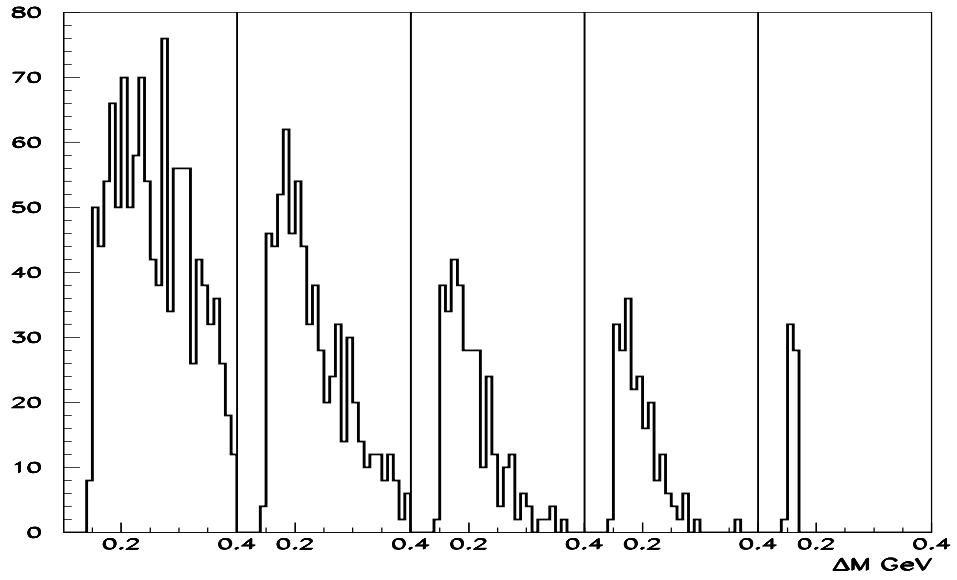

Figure 3.11: Mass difference spectra of decay products calculated in AROMA, in which pion is not emitted in the D^{*-} decay.

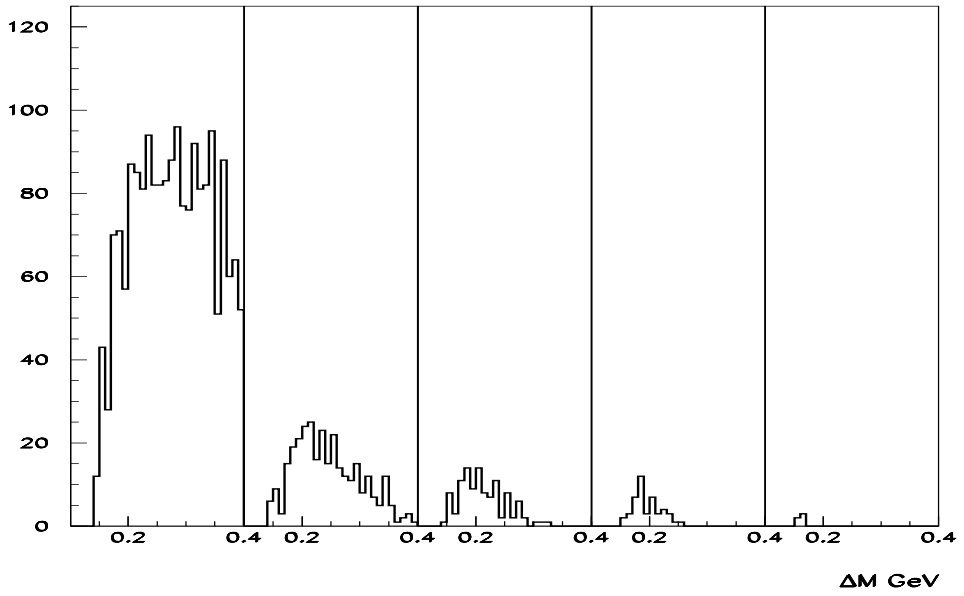

Figure 3.12: Mass-difference spectra for the events tagged as 'non-charm' in PYTHIA after different cuts.

AROMA (signal)	AROMA (π^- not from D^{*-})	PYTHIA (non-charm)	conditions
638	1262	1805	non
594	634	265	A
532	296	91	B
446	194	36	C
298	54	5	$\Delta M < 0.17 GeV$

Table 3.1: Number of events extracted from AROMA and PYTHIA after applying different cuts.

AROMA (signal)	AROMA (π^- not from D^{*-})	PYTHIA (non-charm)	conditions
1000	1000	1000	non
851	502	146	A
833	234	50	B
699	153	20	C
467	42	3	$\Delta M < 0.17 GeV$

Table 3.2: Number of normalized events extracted from AROMA and PYTHIA after applying different cuts.

$p_{K^+} \geq 2$ GeV/c.

In the last linees of tables 3.1 and 3.2 an additional condition $\Delta M < 0.17$ GeV has been applied. This cut is based on the mass-difference spectra shown in figure 3.10, which clearly shows that the yield of the ΔM spectra calculated with AROMA is almost independent of this cut, whereas the yield in the ΔM spectrum extracted from the calculations with PYTHIA is shifted to small values of ΔM with a maximum at $\Delta M = 0.18$ GeV. This shift is partly due to the reduction of the phase-space and partly due to an (unexpected) contribution from kaons with a mass of $\sim$1.5GeV. At $\Delta M \leq 0.17$ GeV the relative background is reduced to a fraction 0.3%, compared to 46.7% for events in which the pion is emitted in the D^{*-} decay.

Chapter 4

The HERMES Experiment

4.1 Introduction

The HERMES (HERa MEasurements of Spin) detector is located in the east sector of the electron(positron)-proton collider at DESY. HERMES only uses the electron beam in combination with a 'fixed' target of polarized or unpolarized gas. The HERMES experiment was designed to determine the spin structure of the proton and neutron by measuring deep-inelastic scattering (DIS) of polarized electrons/positrons from polarized nucleons. First data-taking at HERMES started in 1995 and ended in September 2000. Run number 2 started in 2002, and it is planned to continue until summer 2007.

4.2 The HERA electron-proton collider

HERA consists of two storage rings. The lepton ring (polarized electrons or positrons) has a lenght of 6.3 km and is operated at a fixed energy of 27.5 GeV. In the proton ring protons are being accelerated up to an energy of 920 GeV, with momenta in opposite direction with respect to the electron momenta (Fig. 4.1).

At the start of a fill the electron beam current is about 30 to 40 mA. The average life-time of the beam is approximately 12 hours. In standard operation the beam is dumped at a beam current of about 10 mA. The electrons are stored in 189 bunches with a separation of 96 ns. In the storage ring electrons are polarized in a direction transverse to their momenta due to the Sokolov-Ternov effect [21]. To rotate the electron spin to a direction parallel or antiparallel to their momenta spin rotators are installed in front and behind the HERMES detector. They are build up of interleaved

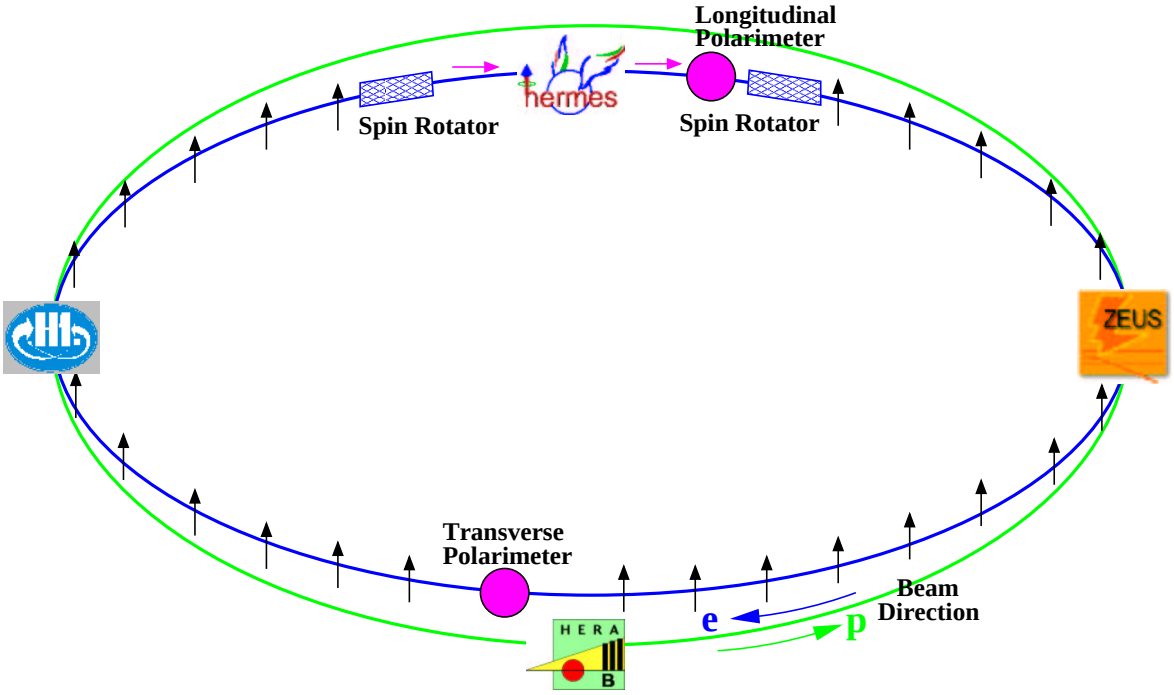

Figure 4.1: The HERA storage ring with the experiments ZEUS, H1, HERA-B and HERMES.

horizontal and vertical dipole magnets. In this way a beam of longitudinal polarized electrons with either negative or positive helicity, is obtained.

The beam polarizations (transverse as well as longitudinal) are measured by a set of Compton polarimeters. The polarimeter for the transversely polarized electrons [31] is located in the west area of HERA.

Both polarimeters use the spin dependence of the cross section for Compton back-scattering of left or right handed polarized laser light from the electrons in the beam. The center of gravity of back-scattered photons is measured by a position-sensitive calorimeter. The top-bottom asymmetry of the position distribution is used to obtain the polarization of the beam [32, 33].

The longitudinal polarimeter (LPOL) [34] is placed in the accelerator tunnel some 50 m down stream of the HERMES experimental area. It has a capability to measure the polarization of individual bunches. Per bunch, thousands of photons are being back-scattered by laser pulses of high intensity and their energy-weighted spin asymmetry is used to derive the beam polarization for each bunch [34]. The average beam polarization of the HERA lepton beam during Run I is in the range 40 - 60 %.

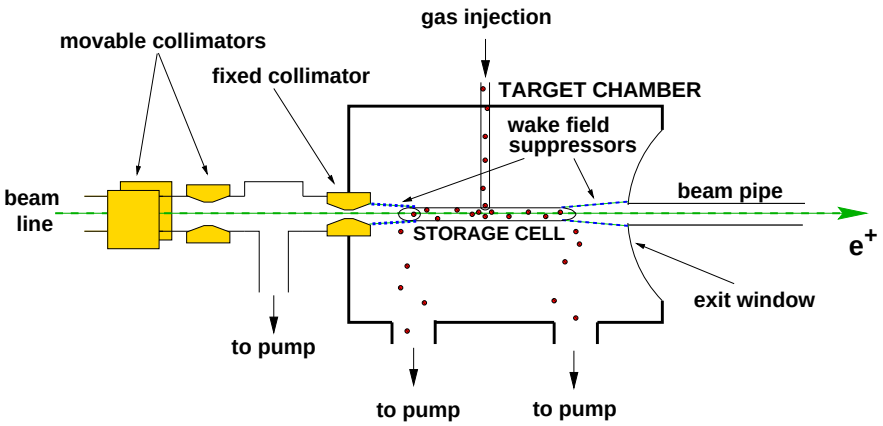

Figure 4.2: Schematic overview of the HERMES target showing the HERA beam-line and storage-cell target.

4.3 Internal gas target

The internal gas target consists of an aluminum tube with a length of 400 mm, a width of 29 mm and a height of 9.8 mm. To increase the target density the diameter of the target cell in the year 2000 was reduced to 21×8.9 mm. It can be filled with polarized or unpolarized gas. The target is positioned in the HERA positron beam. Both ends of the tube are open, such that the electron beam passes through the target cell without interaction with the cell walls (Fig. 4.2).

The polarized ${}^1H$ and ${}^2H$ atoms are produced with an Atomic Beam Source (ABS) [35]. The production process is based on Stern-Gerlach separation of atomic hydrogen or deuterium. The ABS is capable to produce about 6×10^{16} atoms per second for H and 4×10^{16} for D. At a target cell temperature of 100 K the target thickness can reach the value of 10^{14} nucleons/cm^2 for hydrogen and deuterium.

For an unpolarized target, the thickness can be as large as 6 x 10^{15} nucleons/cm^2. This leads to a luminosity of 1.2 x 10^{33} cm$^{-2} \cdot$ s^{-1} at a beam current of 32 mA. Unpolarized data taking is typically used at the end of the fill to collect a large amount of data for unpolarized DIS.

In the storage cell the atoms might be slightly depolarized due to the interactions with the wall. Therefore, the polarization of the target is being controlled permanently. A small fraction of target-gas atoms is analysed in a Breit-Rabi polarimeter [36].

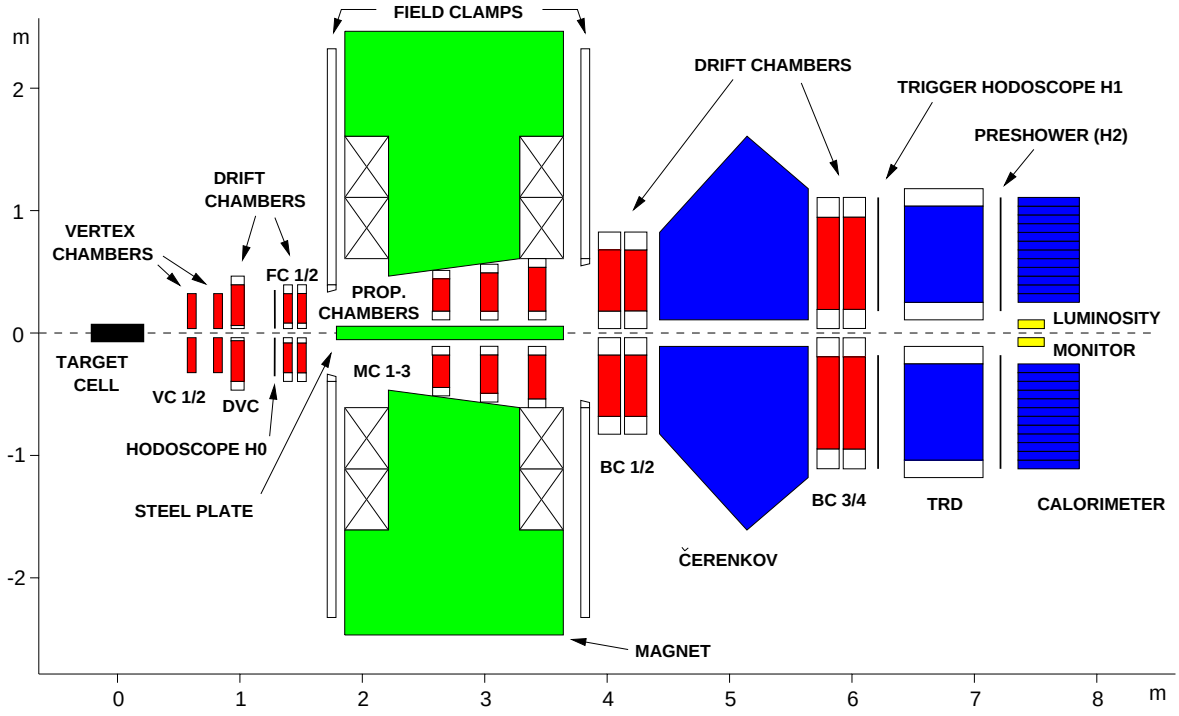

Figure 4.3: Schematic side view of the HERMES spectrometer. The horizontal and vertical scales indicate the sizes in meters.

4.4 The HERMES spectrometer

The HERMES spectrometer is a 'forward-spectrometer'. It is divided in two identical halves, one above and one below the beam. The acceptances in the horizontal and vertical planes are $\theta \leq 170$ mrad and ± 40 mrad $\leq \theta \leq \pm$ 140 mrad. Behind the magnet the horizontal acceptance is increased to 100 mrad.

In the HERMES coordinate system the z-axis is defined in the direction of the lepton beam, the x-axis towards the center of the lepton-ring and the y-axis pointing vertically upwards. The layout of the spectrometer can be divided in three sections, the front region, the magnet and the back region (Fig. 4.3). As compared to the origonal layout shown in Fig. 4.3 a number of modifications have been carried out: 1) the vertex chambers were removed (1998); 2) an array of silicon detectors was installed in the HERMES front region (2001); 3) the Čerenkov detector was replaced by a RICH detector (1998). A detailed description of the HERMES experiment is given in Ref. [37].

Detector	DVC	FC1/FC2	MC1,2,3	BC 1,2,3,4
Dist. from the target (mm)	1 1100	1530,1650	2725,3047,3369	4055,5800
Width of the cell (mm)	6	7	2	15
Resolution ($microns$)	220	225	700	275 / 300

Table 4.1: Main characteristics of the HERMES tracking detectors.

4.5 Tracking detectors

The set of detectors placed in front and behind of the magnet provides the information needed for the reconstruction of the vertex position within the target, the determination of the lepton scattering angle and the emission angles of the created particles. They include the vertex chambers (VC - micro strip gas counters), the drift vertex chambers (DVC) and the front drift chambers (FC). The drift chambers in the back region (BC) and the multi-proportional counters in the magnet (MC) complete the tracking system. Due to radiation damage the VC was removed in 1998. The drift vertex chambers are conventional horizontal-drift type chambers. The efficiency of all chambers is about the same and varies from 96 to 99% for the DVCs and from 98 to 99% for BCs and FCs.

From the coordinates of the interaction points in the 'tracking detectors' in front and behind the magnet first partial tracks are reconstructed by using the 'tree-search algorithm' [29]. All combinations of front and back partial tracks are inspected to determine whether they match the specified tolerance at the $x - y$ plane in the center of the magnet. Those combinations that match are combined to a full track.

The magnet chambers (MC) are used for the reconstruction of the tracks for particles with small momenta that not completely pass the magnet and BC. The magnet chambers are multi-wire proportional chambers. They consist of three modules each: U, X and V. Each submodule consists of an anode plane, a plane at ground potential and two cathode planes.

The reconstructed tracks in HERMES are divided into 'short' and 'long' tracks. The track is named 'long' when it is reconstructed using the information of all tracking chambers, including BC1-4. 'Short' tracks are the tracks of particles, which passed through DVC, FC and MC detectors only (Fig. 4.4).

Some main characteristics of the HERMES tracking detectors are shown in the table 4.1.

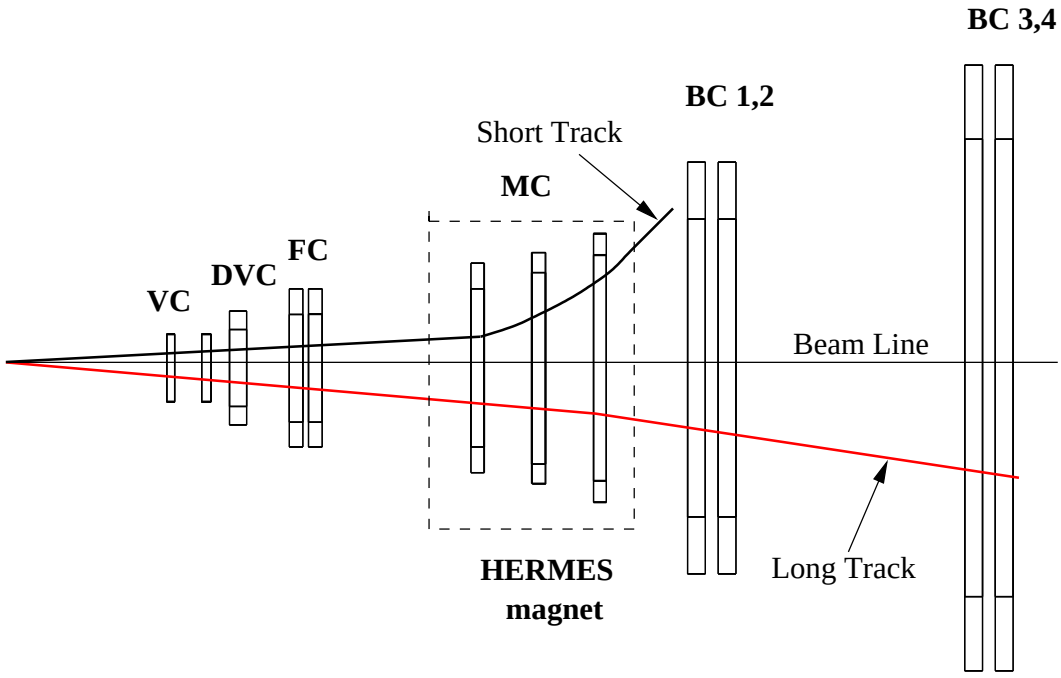

Figure 4.4: Schematic view on the 'long' and 'short' tracks inside the HERMES experiment.

4.6 HERMES Particle Identification Detectors

The HERMES Particle Identification Detector system has been developed to distinguish between leptons, pions and other hadrons. Till 1998 the system consisted of a threshold Čerenkov detector, a transition radiation detector (TRD), a pre-shower counter and an electromagnetic calorimeter. In 1998 the threshold Čerenkov counter was replaced by a Ring-Imaging Čerenkov Detector (RICH). This enables also the identification of pions, kaons and protons [38].

The TRD is composed of 6 modules placed below and above the beam-line. Each module consists of a radiator and a detector. The detectors are proportional chambers filled with a mixture of Xe and CH_4 gas. Two-dimensional matrices of plastic fibers are used as radiator. Electrons (positrons) as well as hadrons deposit energy in the TRD. Since the integrated energy-loss converted into transition radiation is proportional to the Lorentz-factor and electrons have much smaller masses than hadrons the energy-loss dE/dx is larger for electrons than for hadrons. This results in a ratio of the responses of the TRD to electrons and hadrons of about a factor two [39]. Since the spectra are broad and partially overlap information of more modules is used to distinguish between signals from electrons and hadrons. Therefore, the analysis of TRD signals is based on

a truncated mean average method. This method rejects the largest signal produced in the 6 modules and takes the average of the signals from the remaining 5 modules. This suppresses the contribution of high energy hadrons into the lepton energy distribution.

The preshower detector consists of 1 cm of lead and 42 plastic scintillator modules with a width of 9.3 cm each, length of 91 cm and thickness of 1 cm. The radiator initiates electro-magnetic showers. There is a significant difference between the energies deposited by leptons and hadrons in the detector. Since 1 cm of lead corresponds to 0.064 nuclear interaction length hadrons usually induce low ionizing signals in the preshower.

The electromagnetic calorimeter [40] is composed of two arrays of radiation resistant lead glass blocks, one above and one below the beam line. Each block is connected to a photomultiplier tube. The energy resolution of the calorimeter is given by the following parametrization [41]

$$\frac{\sigma(E)}{E}[\%] = \frac{10.0 \pm 2.0}{E[\mathrm{GeV}]} + \frac{5.1 \pm 1.1}{\sqrt{E[\mathrm{GeV}]}} + (2.0 \pm 0.5). \tag{4.1}$$

Before the RICH detector was installed the quantity PID_3 has been used to distinguish tracks from leptons and hadrons,

$$PID_3 = \log_{10} \frac{P^l_{cal} P^l_{pre} P^l_{cher}}{P^h_{cal} P^h_{pre} P^h_{cher}}, \tag{4.2}$$

where ${P_b}^a$ is the conditional probability that the signal of detector b was the response of a particle a passing through the detector. These probabilities are being determined by comparing the detector response functions for every track to the standard detector response function called 'parent distributions'.

Similarly, for the response of the TRD the variable PID_5 is being used,

$$PID_5 = \log_{10} \frac{P^l_{TRD}}{P^h_{TRD}}, \tag{4.3}$$

where P^l_{TRD} and P^h_{TRD} are the sums of the conditional probabilities for detection of leptons and hadrons in the 6 TRD detectors. This particle identification scheme gives a lepton detection efficiency of up to 97% with hadron contamination $\leq 0.01\%$. The hadron detection efficiency is 99% with a contribution of leptons ≤ 0.6 %. The distribution of the PID_3 and PID_5 for lepton/hadron separation is illustrated in Fig. 4.5.

In 1998 the Čerenkov detector was replaced by the RICH. Since then events from leptons and hadrons are separated using PID_2, which is defined similarly as PID_3, but

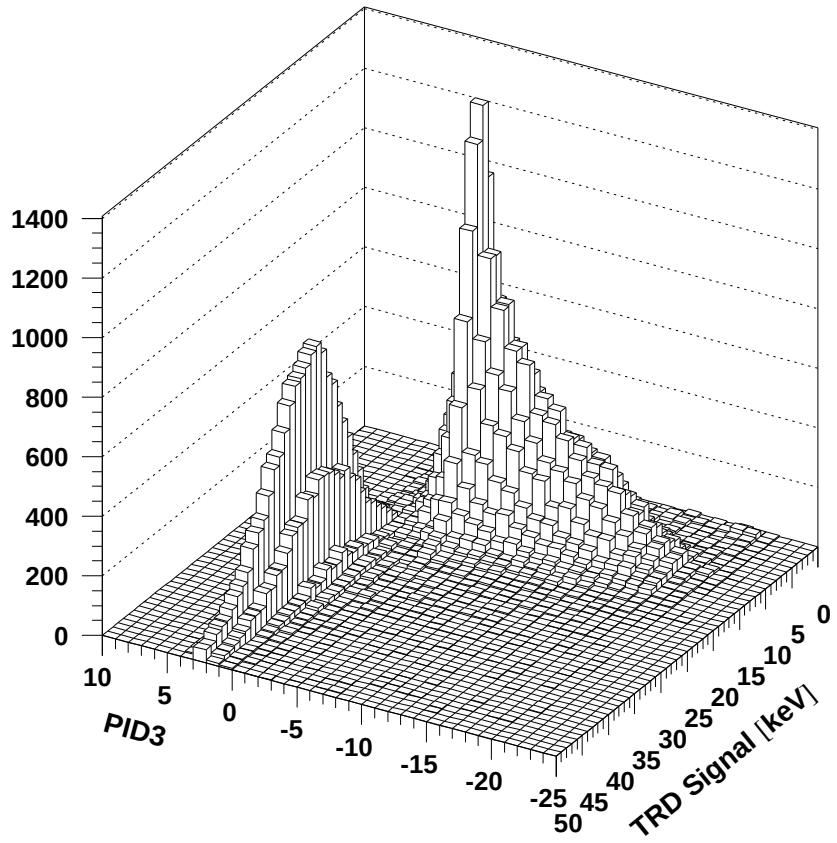

Figure 4.5: Distribution of PID3 and PID5 for separation of leptons (left peak) from hadrons (right peak).

in the definition of PID_2 only information from the calorimeter and the preshower is included, and pion, kaon and proton identification is achieved with the RICH detector.

The RICH is able to identify pions in the momentum range 0.5-16 GeV, kaons between 2 and 16 GeV and protons between 2 and 20 GeV [42] (see Fig. 4.6).

The RICH detector is a dual-radiator detector. Čerenkov light is produced in C_4F_{10} gas and in silica aerogel SiO_2 . It consists of two symmetric (top and bottom) halves installed below and above the beam line.

The Čerenkov photons produced in the aerogel and gas are reflected towards the PMT's by a mirror (Fig. 4.7). Each mirror consists of eight segments which are assembled into 2×4 arrays with radius of curvature 2.2 m.

The emission angles $\cos\theta_C = c/nv$ of the Čerenkov light produced in both radiators are different due to the different refractive indexes for aerogel (1.0014) and the gas (1.03) Ref. [43]. The separation of the various hadrons is based on the difference

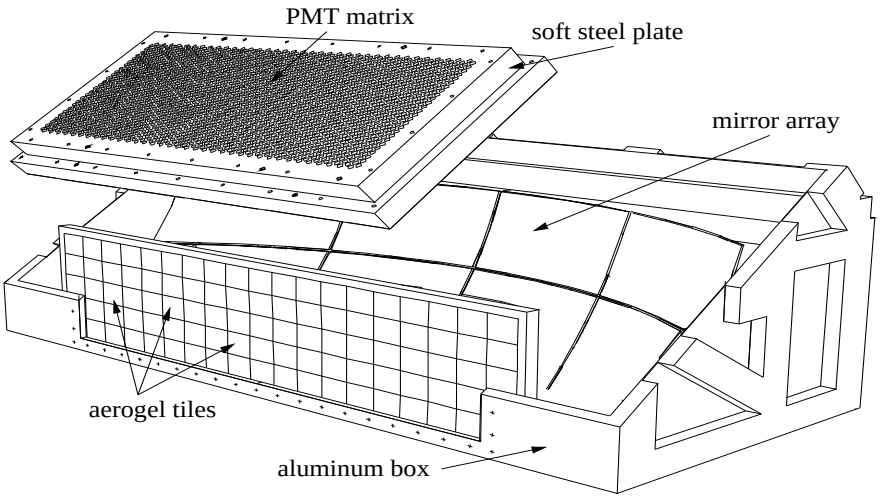

Figure 4.6: A cutaway view of the top half of the RICH detector.

between the Čerenkov angles of the light generated in the detector (Fig. 4.8).

Particle identification with the RICH detector is based on 'inverse ray tracing' (IRT) [44]. This method requires two matrixes. The matrix P_t^i represents the performance of the detector,

$$P(\pi, K, p) = \begin{pmatrix} P_\pi^\pi & P_K^\pi & P_p^\pi \\ P_\pi^K & P_K^K & P_p^K \\ P_\pi^p & P_K^p & P_p^p \\ P_\pi^X & P_K^X & P_p^X \end{pmatrix}. \tag{4.4}$$

The diagonal matrix elements $(P_\pi^\pi, P_K^K, P_p^p)$ represent the probabilities that the incident hadron (π, K, p) is properly identified. The non-diagonal elements in the first three rows are inefficiencies in detecting the respective hadron, and the last row accounts for the non-identified particles.

The elements of the P-matrix are obtained from a Monte-Carlo simulation of the emission angles of the Čerenkov light produced by various particles in a wide range of momenta.

From the P-matrix the complimentary matrix $Q(\pi, K, p)$ can be calculated,

$$Q(\pi, K, p) = \begin{pmatrix} Q_\pi^\pi & Q_\pi^K & Q_\pi^P & Q_\pi^X \\ Q_K^\pi & Q_K^K & Q_K^p & Q_K^X \\ Q_p^\pi & Q_p^K & Q_p^P & Q_p^X \end{pmatrix}. \tag{4.5}$$

The labeling of the matrix elements is the same as for the P matrix. The 'real'

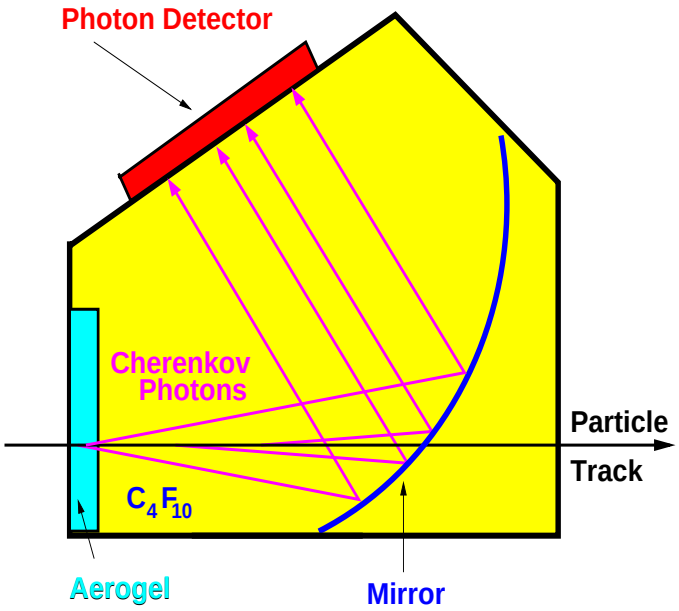

Figure 4.7: Čerenkov light photons produced in the aerogel and in the gas form ring images that are reflected to the PMT matrix.

yield of the various hadrons $\overrightarrow{N}(N_K, N_p, N_\pi)$ is extracted from the measured ones $\overrightarrow{I}(I_K, I_p, I_\pi, I_X)$ according to

$$\overrightarrow{N} = Q \cdot \overrightarrow{I} \tag{4.6}$$

4.7 The Luminosity Monitor

To extract the asymmetry from the data taken with different beam/target polarizations the measured number of events has to be normalized to the integrated luminosity. For a fixed target experiment the luminosity can be calculated as follows

$$L \equiv \phi_b N_T, \tag{4.7}$$

where ϕ_b is the flux of the beam particles and N_T is the number of target nuclei per cm^2 within the cross section of the beam. The measurement of ϕ_b is based on elastic scattering of the beam leptons from electrons in the target gas. For an electron beam Moller scattering takes place: $e^-e^- \rightarrow e^-e^-$. If a positron beam is used the scattering process $e^+e^- \rightarrow e^+e^-$ (Bhabha scattering) is followed by the annihilation of electron-

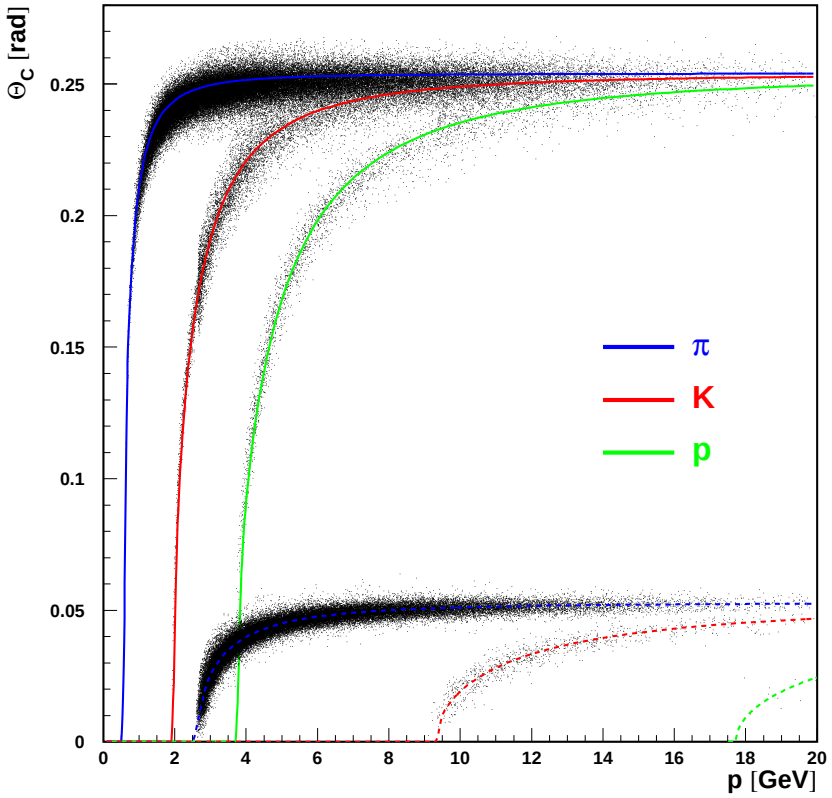

Figure 4.8: Reconstructed Čerenkov angles versus the momenta of hadrons for aerogel (top three) and gas radiators (bottom three).

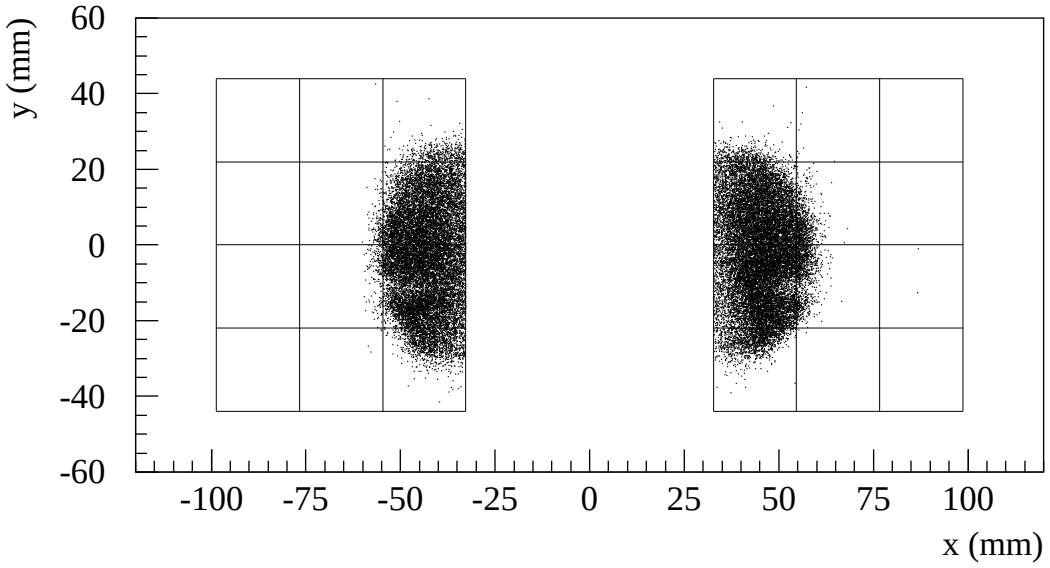

Figure 4.9: Hit distribution in the luminosity monitor.

positron pair into photon pairs $e^+e^- \rightarrow \gamma\gamma$. The cross section of both processes is known from QED. For this purpose a calorimeter named the luminosity monitor is installed 7.2 m downstream of the center of the target to the left and right sides of the beam pipe. Both calorimeter modules consist of 12 NaBi $(WO_4)_2$ crystals which have high radiation hardness. This is required because of the high radiation background in the detector region [45].

The typical hit distribution in the calorimeters of the luminosity monitor is shown on Fig 4.9.

4.8 Trigger and Data Acquisition

The HERMES first-level trigger system is used for the selection of different types of events and to suppress events generated by background radiation. The triggers correspond to deep-inelastic scattering and quasi-real photoproduction processes. Additional triggers are being used for detector monitoring and calibration.

The deep-inelastic scattering trigger is activated when a hit takes place in all three (H0, H1, H2) hodoscopes and when in addition an energy of at least 3.5 GeV is deposited in two adjacent columns of the calorimeter. The timing of the electron bunches is taken as a clock for the trigger synchronization. In the measurements with a polarized target the calorimeter threshold was set at 1.4 GeV. These requirements suppress the rate of hadronic background.

The photo-production trigger uses signals from hadrons produced in electron-nucleon scattering at low Q^2 and their decay to two or more particles. The trigger requires a charged particle track in both halves of the spectrometer within the time interval set by the HERA-clock, all hodoscopes and the drift chambers behind the magnet (BC). The last requirement rejects triggers generated by particles produced in collimators up stream of the electron beam.

When the trigger makes a positive decision the HERMES Data Acquisition system starts the read-out of the information of all the detectors related to the event.

The collected data are processed by a fastbus system and can be compressed by a factor of two. Data are being recorded on a taping robot and backed up locally to another tape. Writing takes place between two HERA fills.

To make the data storage less complicated the data taking is organised as 'run-to-run' recording. In each run about 60 MB of data is recorded. The time needed to complete a run depends on the beam and the target conditions. In experiments with the polarized target the time is longer than in experiments with an unpolarized target, because the lower target densities correspond to lower trigger rates even with the lower threshold of the calorimeter.

Chapter 5

Data Analysis

5.1 Introduction

The results of the Monte Carlo calculations, performed with programs AROMA and PYTHIA, predict that the fraction of the events originating from D^{*-} decay in the data is small [8, 46, 47]. Using the Monte Carlo calculations, several tools have been developed to reduce the background in the reconstructed $\bar{D}^0$ and D^{*-} mass and mass-difference $\Delta M = M(D^{*-}) - M(\bar{D}^0)$ spectra for semi-leptonic decay of the D^{*-}. These tools are applied in the data analysis discussed in this chapter.

The data used in this analysis were taken in 1999 and 2000. The target was polarized deuterium. As mentioned in chapter 4, the target density was increased in 2000 by reducing the diameter of the target cell. Furthermore, the intensity of the positron beam was improved in the year 2000, which also led to an increase of the luminosity. Therefore, the majority of the events used in this analysis were taken in 2000. The data taken in both years were analysed separately.

The strategy followed in the data analysis is in accordance with the one applied to the Monte Carlo calculations discussed in chapter 2. However, firstly a set of data-quality requirements are applied to the data and lower thresholds are set on the electron, pion and kaon momenta. Next, the coordinates of the interaction point and the minimum distances between the electron, kaon and pion momenta are determined. Events are only accepted for further analysis if the interaction point is within the target and the minimum distance between the momentum vectors is smaller than a given value. The data-quality requirements and momentum cuts are discussed in sections 5.2, and vertex-reconstruction of the three particles in section 5.3.

Then, in section 5.4, the $e^- K^+$ and $\pi^- e^- K^+$ invariant masses, and the $(\pi^- e^- K^+) - (e^- K^+)$ mass differences are extracted from the selected events.

Criterion	Requirements
Target type	Polarized deuterium or proton
Beam polarization	$0.3 \leq \lvert P_{beam} \rvert \leq 0.8$
Target polarization	$0.8 \leq \lvert P_{target} \rvert \leq 0.99$
First burst	Reject
Burts length	$0s \leq \Delta_{burst} \leq 11s$
Luminosity trigger rate	7.5Hz$\leq L \leq$ 1250Hz
DAQ efficiency	$0.6 \leq \lvert e_{daq} \rvert \leq 1$

Table 5.1: Data quality requirements for the 1999-2000 data set.

The interpretation of the obtained mass spectra is presented and discussed in chapter 6. From least-square fits of the calculated ΔM spectra to the data the number of events that can be attributed to D^{*-}-decay is determined for the two directions of the target polarisation. From these numbers the double-spin asymmetry is extracted.

5.2 Data selection

The quality requirements applied to the data are given in table 5.1. They include the conditions set to beam and target polarisation, the structure of the electron burst and the data aquisition system.

Fig. 5.1 shows the momentum distributions of the three particle types. For each of the particles involved the ranges of their momenta are reduced, either due to the thresholds set by the detector or by cuts on the data. The latter are based on the results of the Monte Carlo calculations. The lower limit of the electron momentum of 1.5 GeV is determined by the energy threshold of the trigger. Similarly, the RICH detector determines the lower limits of the kaon and pion momenta of 2 GeV and 0.6 GeV, respectively. Furthermore, the results of the Monte Carlo calculations indicate that pions emitted in the decay of the D^{*-} have a maximum momentum of about 2 GeV. Therefore, an upper threshold is set on the pion momentum.

In table 5.2 the thresholds set for the momenta of these three particle types are summarized.

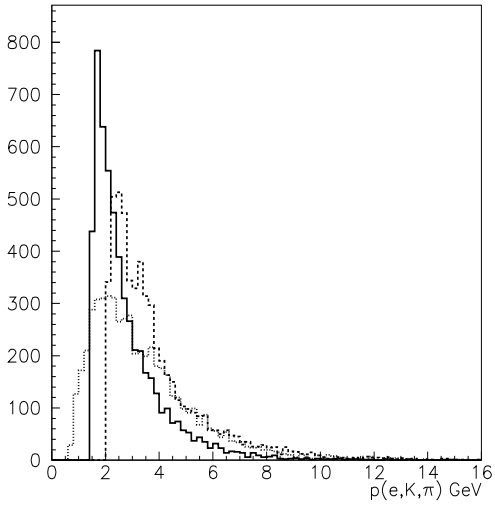

Figure 5.1: Momentum distributions of e^- (solid histogram), K^+ (dashed histogram), π^- (dotted histogram).

particle	momentum (GeV)	selection based on :
e^-	$p_{e^-} \geq 1.5$	threshold calorimeter
K^+	$p_{K^+} \geq 2$	minimum momentum in RICH
π^-	$p_{\pi^-} \leq 2$	Monte Carlo calculations

Table 5.2: The thresholds set for the momenta of these three particle types are summarized.

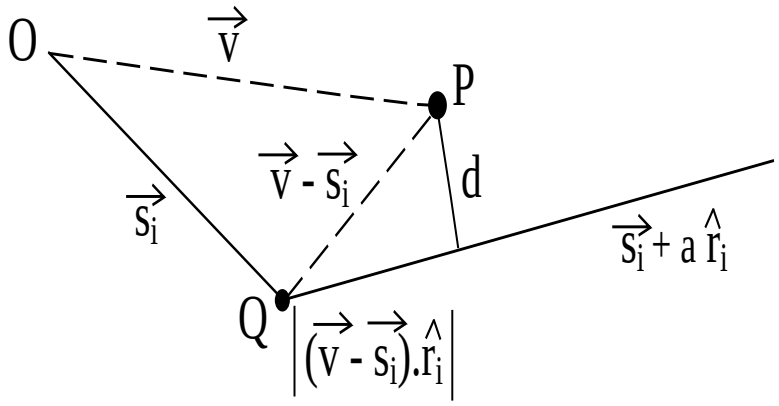

Figure 5.2: Distance (d) from a space point P(x,y,z) to a track with origin in Q and direction $\hat{r}_i$.

5.3 Vertex reconstruction

The lifetimes of the D^{*-} and its decay products are negligible as compared the time they need to leave the target. Therefore, tracks of all three particles are required to originate from the target domain. In addition to this standard procedure, it is required that the momenta of the e^-, K^+ and π^- have a common vertex within the target. This vertex has been reconstructed from the momenta of these three particles by minimizing their distances to an abitrary space point $P(\vec{v})$, with $(\vec{v} = x, y, z)$ (Fig. 5.2).

Defining a track originating from a point $Q(\vec{s}_i)$ in a coordinate system with origin in O as $\vec{s}_i$ + a $\hat{\mathbf{r}}_i$, where $\hat{\mathbf{r}}_i$ is the unit vector in the direction of the momentum of the particle, the distance of the tracks to an arbibitrary $P(\vec{v})$ is given by

$$d_i(\vec{v}) = \sqrt{(\vec{v} - \vec{s}_i)^2 - ((\vec{v} - \vec{s}_i).\hat{\mathbf{r}}_i)^2}. \tag{5.1}$$

Then, the quadratic sum of the distances of the three tracks to P is given by $\Sigma_i(d_i(\vec{v}))^2$. This sum is minimal when [29]:

$$\nabla_{\vec{v}} \Sigma_i (d_i(\vec{v}))^2 = 0 \tag{5.2}$$

After taking the derivatives one obtains the equation

$$\Sigma_i[(\vec{v} - \vec{s}_i) - \hat{\mathbf{r}}_i.(\vec{v} - \vec{s}_i)] = 0, \tag{5.3}$$

or equivalently a set of linear equations. The coordinates of the reconstructed interaction point are obtained by solving this set of equations. In figure 5.3 the distributions of the x and y-coordinates of the interaction point are shown. For almost all events

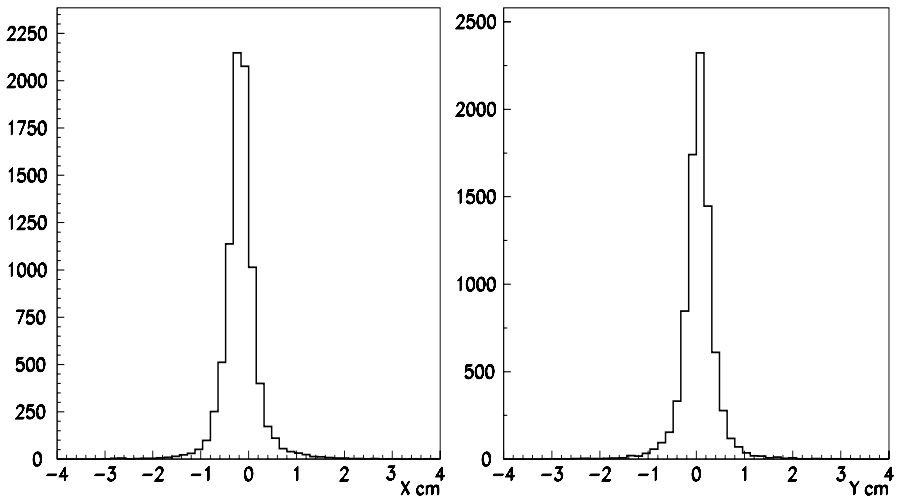

Figure 5.3: The distribution of x and y coordinates of the interaction point $P(x, y, z)$, extracted from the minimum distance from a space point P to the electron, kaon and pion momenta .

this interaction point is within the target cell. The distributions of the (minimum) distances between the tracks at this space point $P(x, y, z)$ are shown in figure 5.4. The three distributions indicate that for almost all events the three particles have a common vertex. The area left of the vertical lines in the three figures mark the data that are accepted for further analysis. This includes the events for which all three distances are smaller than one centimeter.

5.4 Data selection using the results of the Monte Carlo Calculations

Figure 5.5 shows the invariant mass spectra for the e^-K^+ and $\pi^-e^-K^+$ systems and the reconstructed mass difference spectrum $\Delta M = M_{\pi^-e^-K^+} - M_{e^-K^+}$, extracted from the data after applying the cuts on the momenta and putting limits to the reconstructed minimum distances between the electron, kaon and pion momenta at the interaction vertex. Only events up to $\Delta M = 0.4$ GeV are included in this spectrum. According to the results of the calculations performed with AROMA a small fraction of 0.2 % of the events from D^{*-}-decay is beyond this range in ΔM (section 3.3).

The solid histogram in figure 5.5 shows the mass-difference spectrum ΔM without any conditions applied, and the shaded area the spectrum with the additional constraint on the interaction vertex.

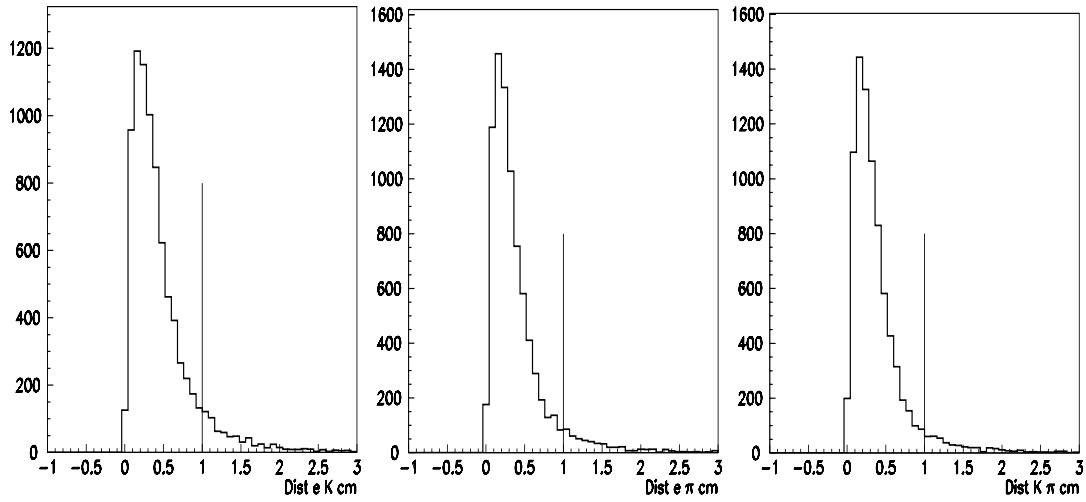

Figure 5.4: Minimum distances between e^- and K^+, e^- and π^-, and K^+ and π^- momentum vectors. The lines at a distance of 1 cm indicate the cuts made in the analysis.

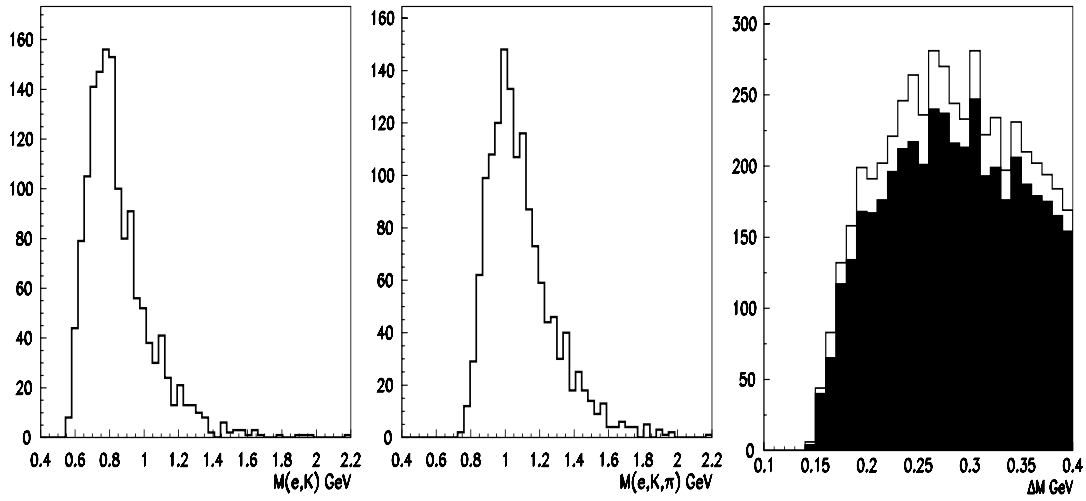

Figure 5.5: Reconstructed $M_{e^-K^+}$ and $M_{e^-K^+\pi^-}$ mass spectra and $\Delta M = M_{e^-K^+\pi^-} - M_{e^-K^+}$ mass difference spectrum. Dark area indicates ΔM spectrum after cuts in minimum distances applied.

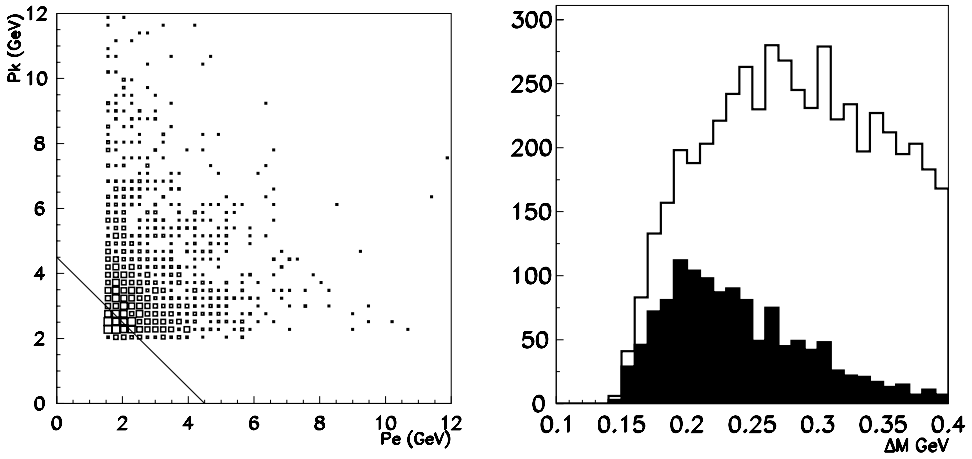

Figure 5.6: The distribution of the kaon versus the electron momentum (left histogram) and the ΔM spectrum (right histogram). In the latter spectrum, the open histogram includes all data, while in the one given by the shaded histogram only the events for which $p_e + p_K > 4.5\,\mathrm{GeV}$ applies are shown.

By comparing this spectrum with that obtained from the Monte Carlo calculations performed with the programs AROMA (figure 3.3) and PHYTHIA (figure 3.4) it is evident that it is dominated by the background. The shapes as well as the maximum of the distribution are similar as those calculated with PYTHIA. This is not surprising because the results from PYTHIA indicate that the fraction of the events from D^{*-}-decay is small compared to the fraction from other processes. Although there are uncertainties in the cross sections for production of charmed mesons near threshold in PYTHIA, implying that the fraction from D^{*-} decay may be somewhat larger, it is clear that a strong reduction of the background is needed in order to extract information on D^{*-}-decay from the data. This background reduction is achieved by applying various cuts on the data according to the results of the Monte Carlo calulations. In the following this background reduction is discussed step by step. As in the Monte Carlo calculations firstly a minimum value has been required for the sum of the kaon and electron momenta, $p_{K^+} + p_{e^-} \geq 4.5$ GeV (Fig. 5.6 left). The effect on the ΔM spectrum is shown in Fig. 5.6 (right). Similarly as in the previous figure, the open and the shaded histograms correspond to the spectra without and with this cut. The difference in the shape of both spectra of figure 5.6b reflects a strong reduction of the data at larger values of ΔM, whereas at small ΔM the reduction is much less. At $\Delta M \leq 0.2$ the reduction is 45 %, whereas at $\Delta M \geq 0.2$ this is 88 %. This effect can

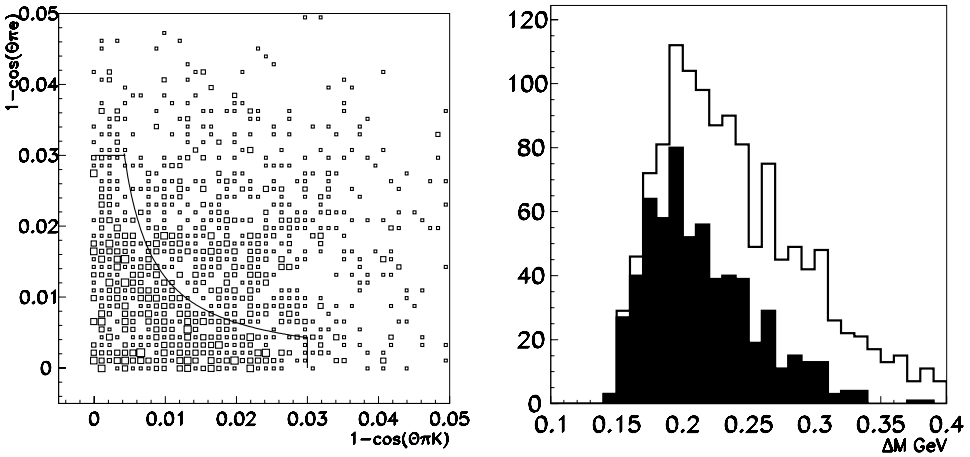

Figure 5.7: The distribution $1-\cos(\theta_{p_{K^+}p_{\pi^-}})$ versus $1-\cos(\theta_{p_{e^-}p_{\pi^-}})$ (left) and the ΔM spectrum (right) before (open histogram) and after (shaded histogram) the reduction of the ranges of the emission angles. Details are given in the text.

be interpreted as follows. Firstly, the lower limit on the sum of the electron and kaon momenta reduces the phase space in such a way that the number of events with large ΔM is suppressed. Secondly, according to the calculations with AROMA the number of events from D^{*-} decay, which are concentrated at small ΔM, is hardly changed.

In the next step of the analysis the range in emission angles of the electron and kaon momenta with respect to the pion momentum was reduced. Events were only accepted if $(1-\cos(\theta_{p_{K^+}p_{\pi^-}})) < 0.03$, $(1-\cos(\theta_{p_{e^-}p_{\pi^-}})) < 0.03$ and

$(1-\cos(\theta_{p_{K^+}p_{\pi^-}})) \times (1-\cos(\theta_{p_{e^-}p_{\pi^-}})) < (0.016)^2/2$ (figure 5.7 left histogram).

In figure 5.7 (right), the spectra before and after applying these cuts are indicated by the open and shaded histogram, respectively. The effect of this cut on the ΔM spectrum is similar to that of the previous one, but the effect is more significant. The intensity at $\Delta M \leq 0.2$ GeV is hardly reduced and a strong reduction is observed at larger values of ΔM.

The last step in the reduction of the background includes constraints on the pion momentum and the invariant mass $M_{e^-K^+}$. The upper values set to both quantities are indicated in figure 5.8 (left). The result is shown in figure 5.8 (right). It is clear that not only the yield for $\Delta M \geq 0.2$ is reduced, but also for smaller values of ΔM. However, this not necessarilly implies a reduction of the number of events from D^{*-} decay. Note that calculations performed with AROMA do not predict such a reduction.

Figure 5.9 shows the ΔM spectra obtained after the subsequent steps in the data

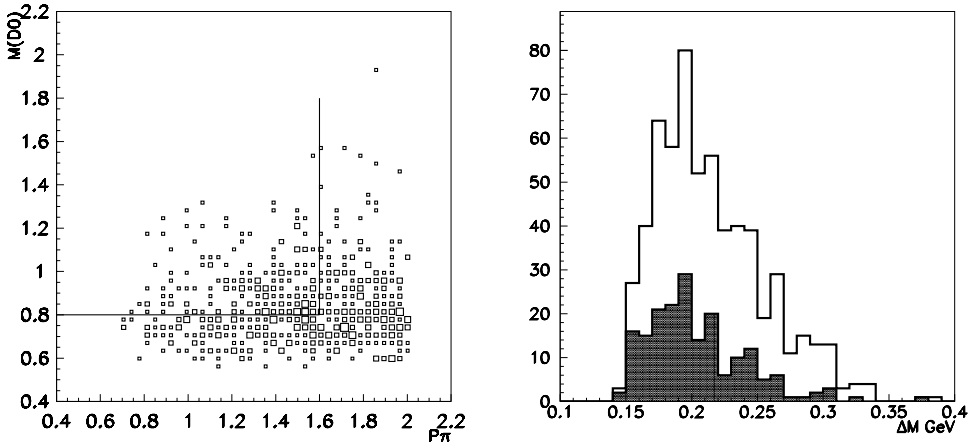

Figure 5.8: Reconstructed invariant mass of the (K^+e^-) system '$M(D^0)$' versus the momentum of the pion p_{π^-} (left histogram) and the ΔM (right histogram shaded area) spectrum, in which only events with $p_\pi \leq 1.6$ GeV and $M_{D^0} \geq 0.8$ are included.

analysis. This figure can be compared directly to the figures 3.10 and 3.12, where similar spectra are presented for the Monte Carlo data obtained from calculations with AROMA and PYTHIA, respectively. They indicate a further concentration of the events in the domain of small values of ΔM at each step of the data reduction. Finally, only events are left in the domain where events from D^{*-} decay are expected.

In table 5.3 the number of events in the ΔM spectra, obtained after the subsequent steps in the data reduction, is presented. This gives a more quantitative impression of the composition of the ΔM spectra. The data are presented for three bins in ΔM. They cover the ranges $0.14 - 1.6$ GeV, $0.14 - 0.4$ GeV and $0.14 - 0.2$ GeV. According to the Monte Carlo calculations the fraction of the events from D^{*-} decay should increase when the upper limit in ΔM is decreased. The final data sample contains only 187 events in the range $0.14\text{GeV} \leq \Delta\text{M}_1 \leq 0.4\text{GeV}$ as well as in the range $0.14\text{GeV} \leq \Delta\text{M}_2 \leq 1.6\text{GeV}$. This number is 105 events in the spectrum ΔM_3, in which the upper limit is reduced to 0.20 GeV.

Hence, in the total range of ΔM included in the analysis $\Delta M_1 = 0.14$ - 1.6 GeV only about 2% of the data is left. In the range $\Delta M_2 = 0.14$ - 0.4 GeV this fraction is 4% and in the smallest range of $\Delta M_3 = 0.14$ - 0.2 GeV, where according to the calculations performed with AROMA the events from D^{*-} decay are concentrated, this is 17%. The calculation with AROMA predicts that in the latter two ΔM regions after all cuts the number of events from D^{*-} is reduced by 50 % and 15 %, respectively.

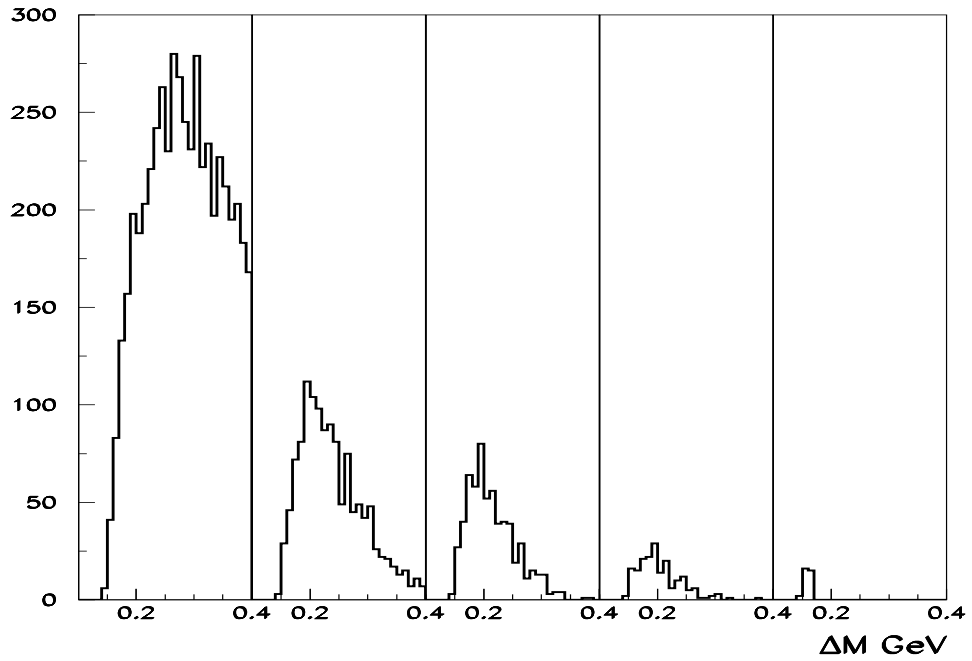

Figure 5.9: The ΔM spectra after applying the successive cuts.

This leads to the conclusion that the background reduction was effective. Nevertheless, according to the results of the Monte Carlo calculations, a sizeable fraction of the ΔM_2 and ΔM_3 domains still stems from the background.

A comparison of the measured ΔM spectra with those from the Monte Carlo calculations clearly indicates a systematic increase of the fraction from D^{*-} decay. However, it does not give quantitative information on this fraction. Therefore, it is difficult to draw conclusions about the ratio of events from D^{*-} decay and background based on the shape of the ΔM spectrum.

Furthermore, one has to be careful in drawing conclusions from the shape of this spectrum, because the various cuts reduce the phase-space for the combination of electron/kaon/pion momentum and this leads to a shift of the maximum in the ΔM spectrum to smaller values. In the next section, the unfolding procedure used to determine the number of the events stemming from D^{*-}-decay is discussed and the results are presented.

Data taken in 2000			Condition
ΔM_1	ΔM_2	ΔM_3	
8258	5109	618	none
1287	1250	343	$p_{\pi^-} < 2\,\mathrm{GeV},\ p_{e^-} > 1.5\,\mathrm{GeV}$ $p_{e^-} + p_{K^+} \geq 4.5\,\mathrm{GeV}$
613	611	272	and $1 - cos(\theta_{p_{K^+} p_{\pi^-}}) < 0.03, 1 - cos(\theta_{p_{e^-} p_{\pi^-}}) < 0.03$ $1 - cos(\theta_{p_{K^+} p_{\pi^-}}) \times 1 - cos(\theta_{p_{e^-} p_{\pi^-}}) < (0.016)^2/2$
187	187	105	and $M(K^+ e^-) > 0.8\,\mathrm{GeV},\ p_{\pi^-} < 1.6\,\mathrm{GeV}$

Table 5.3: Number of events in the ΔM spectrum after various steps in the data selection. The range spanned in the ΔM_1 spectrum is (0.14 - 1.6) GeV, that for ΔM_2 (0.14 - 0.4) GeV and for ΔM_3 (0.14 - 0.2) GeV.

Chapter 6

Results and Discussion

6.1 Extraction of the number of events from D^{*-}-decay

In order to make a decomposition of the ΔM spectrum into the contributions from D^{*-}-decay and other processes, the measured ΔM spectra have to be compared with the spectra calculated with the programs AROMA and PYTHIA in a quantitative way. There are several options to make such a comparison.

1. Extract from the Monte Carlo calculations performed with PYTHIA the contributions to the ΔM spectrum from D^{*-}-decay and other processes, respectively. Normalize these calculated spectra to the data and determine the fractions from the decay of charmed mesons and other processes. Since the contribution from the D^{*-}-decay is expected to be small, large amounts of Monte Carlo data have to be generated. This is time consuming. Furthermore, one has to rely on the cross sections for the production of charmed mesons in PYTHIA at energies in the range covered by the HERMES experiment.

2. Combine the contributions to the ΔM spectrum from D^{*-}-decay calculated with AROMA and from the background extracted from the calculations with PYTHIA (the events from D^{*-} decay in PYTHIA are not taken into account). Again one has to rely on the cross sections for creation of charmed mesons. The number of Monte Carlo data presented in chapter 3 are sufficient for such an analysis.

3. Use, as in option 2, the Monte Carlo data for the production of charmed mesons and the background from the calculations performed with AROMA and PYTHIA, respectively. Fit these spectra to the data. Perform these fits at each step of the analysis. An argument in favour of this method is the fact [10] that considerable

uncertainties exist in the cross section for charm production by PYTHIA or AROMA.

In this thesis, the last method is applied. The function fitted to the data is

$$N_{predicted} = x \times N_{AROMA} + y \times N_{PYTHIA}, \tag{6.1}$$

where x and y are free parameters. By fitting the Monte Carlo spectra to the data at each of the three steps in the data analysis given in table 6 the consistency in the analysis has been checked and the contribution of D^{*-}-decay to the three ΔM spectra has been determined.

It is convenient to rearrange Eq. (6.1) such that the two parameters account for a normalization constant and the fraction of D^{*-}-decay in the ΔM spectrum.

This gives

$$\begin{aligned} N_{predicted} &= x \times N_{AROMA} + y \times N_{PYTHIA} && (6.2)\\ &= y \times (\frac{x}{y} \times N_{AROMA} + N_{PYTHIA}) && (6.3)\\ &= N \times (f \times N_{AROMA} + N_{PYTHIA}), && (6.4) \end{aligned}$$

with $N = y$ and $f = \frac{x}{y}$.

Assuming that AROMA properly describes the production of charmed particles and PYTHIA the background, the constant N normalizes the Monte Carlo spectra to the data and does not change in the various steps of the analysis, while the parameter f accounts for the fraction of the data that can be attributed to D^{*-}-decay. Hence, by fitting the three ΔM spectra corresponding to the three conditions listed in table 6.1 the fraction of events from D^{*-}-decay is obtained.

Note that f is not equal to the fraction from D^{*-}-decay, but a parameter that is proportional to that fraction. At each step the decomposition of the data in events from D^{*-}-decay and background is given by

$$\begin{aligned} N_{predicted} &= N_{charm} + N_{background} && (6.5)\\ &= N \times f \times N_{AROMA} + N \times N_{PTHIYA}. && (6.6) \end{aligned}$$

From the Monte Carlo calculations it is known that the contribution of D^{*-}-decay to the ΔM spectrum is small when no restrictions are made to the data. This contribution is negligible if $\Delta M \geq 0.20$ GeV. In this domain there is only a very small contribution from the decay $D^{*-} \rightarrow \pi^0 D^- \rightarrow \pi^0 \pi^- e^- K^+ \bar{\nu}$. Therefore, f is taken zero in this spectrum and the normalization constant N was extracted from a fit of the "background

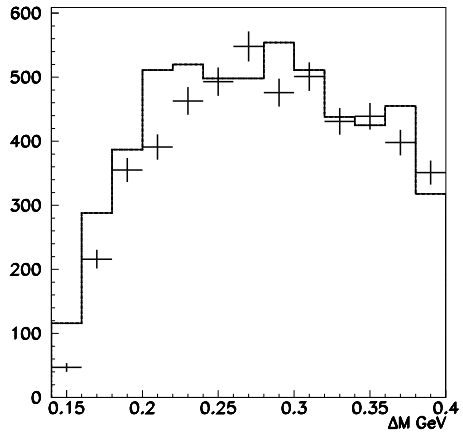

Figure 6.1: Distribution of normalized ΔM spectrum calculated with the program PYTHIA (solid histogram) and the data points. The fit is performed in the range $0.20 \leq \Delta M \leq 0.4$ GeV.

spectrum" calculated with PYTHIA to the data in the range $0.20 \leq \Delta M \leq 0.4$ GeV. The upper limit was set on 0.4 GeV since the statistical accuracy in the ΔM spectrum calculated with PYTHIA reduces rapidly above this value after As before, only events with electron, kaon and pion multiplicity equal to one were included and constraints were set to the interaction vertex (section 5.3). In figure 6.1 the data and the calculated spectrum, multiplied with the normalization factor $N = 4.4$ extracted from the fit, are shown. Using this normalization factor, the contribution of D^{*-} decay, expressed in the factor f, was determined for the lower ΔM region ($0.14 \leq \Delta M \leq 0.20$ GeV).

In figure 6.2 the fits to the three spectra are shown, and in table 6.1 the parameters N and f extracted from the fits are listed. The spectra labeled as A, B and C are reproduced reasonably well by those obtained from the Monte Carlo calculations. Deviations are seen at high ΔM values, which is largely due to an overestimate of the data in the last channel by the calculated spectrum. If the range is reduced to 0.14-0.19 GeV the results of the fit to spectrum B are $\chi^2 = 1.1$ and $f = 0.026$. Using the factors f obtained from the fits to the data listed in table 6.1, the decomposition of the yield in events from D^{*-}-decay and background listed in table 6.2 is obtained.

Although the fitted combinations of AROMA and PYTHIA Monte Carlo spectra do not give an excellent description of the measured ΔM spectra, they do account for the gross features. At large ΔM the PYTHIA background is dominant, whereas at small ΔM the charm part contributes significantly. Moreover, the number of charm events extracted (see table 6.2) is consistent whatever cut (A, B or C) is applied. This

Results from fit			Condition	
N	f	χ^2		
4.4	0.017±0.01	0.4	$p_{\pi^-} < 2\,\mathrm{GeV},\ \mathrm{p_{e^-}} > 1.5\,\mathrm{GeV}$ $p_{e^-} + p_{K^+} \geq 4.5\,\mathrm{GeV}$	A
4.4	0.022±0.009	5.6	and $1-\cos(\theta_{p_{K^+}p_{\pi^-}}) < 0.03, 1-\cos(\theta_{p_{e^-}p_{\pi^-}}) < 0.03$ $[1-\cos(\theta_{p_{K^+}p_{\pi^-}})] \times [1-\cos(\theta_{p_{e^-}p_{\pi^-}})] < (0.016)^2/2$	B
4.4	$0.018^{+0.01}_{-0.005}$	1.6	and $M_{K^+e^-} > 0.8$ GeV, $\mathrm{p_{\pi^-}} < 1.6\,\mathrm{GeV}$	C

Table 6.1: Results from fits of the calculated ΔM spectra to the data showing the normalization factor and fit parameters obtained for each condition.

Results from fit $\Delta M = 0.14 - 0.20$ GeV					
charm	background	sum	$F = \frac{charm}{sum} \times 100\%$	data	Condition
52	252	304	17 %	343	A
67	163	230	29 %	272	B
40	92	132	30 %	197	C

Results from fit $\Delta M = 0.14 - 0.17$ GeV					
charm	background	sum	$F = \frac{charm}{sum} \times 100\%$	data	Condition
31	57	88	35 %	78	A
42	39	81	52 %	70	B
33	13	46	72 %	33	C

Results from fit $\Delta M = 0.17 - 0.20$ GeV					
charm	background	sum	$F = \frac{charm}{sum} \times 100\%$	data	Condition
21	195	216	10 %	265	A
25	124	149	17 %	202	B
7	79	86	8 %	164	C

Table 6.2: Results from fits of the calculated ΔM spectra to the data showing the decomposition of the yield in events from D^{*-}-decay and background for each condition and different ΔM ranges.

consistency gives confidence to the analysis and enables us to consider the double spin asymmetries.

The number of events from D^{*-}-decay follows directly from equation (6.6), with N and f are taken from table 6.1. It is clear that the fraction of events originating from D^{*-}-decay systematically increases in the subsequent steps in the data reduction, and that this fraction is systematically larger when the range in ΔM is reduced to 0.14 - 0.17 GeV. However, when the maximum fraction of 72 % is reached the spectrum contains only 46 events, of which 33 events can be attributed to the decay of the D^{*-} meson.

6.2 Double-spin asymmetry

The motivation of this study is the extraction of the double-spin asymmetry for events from D^{*-}-decay. From the Monte Carlo calculations it follows that in the ΔM spectrum these events are concentrated at $\Delta M \leq 0.17$ GeV. Qualitative information on the asymmetry is obtained by comparing the number of events in this domain at two values of the beam-target polarisation. Such a comparison is made in figure 6.3. In the upper part of this figure the data obtained at anti-parallel and parallel beam-target spins (solid histogram) are compared with the spectrum obtained from calculations with AROMA (dashed histograms). The data measured in 1999 and 2000 are added. The dashed histogram in both figures is the same as the one shown in Fig. 3.10, but scaled by a factor 0.6. This factor accounts for the contribution of the data taken in 1999 (factor 1.2), and the splitting into 2 subsets (factor 0.5). It is assumed that in the data taken in 1999 the fraction of events from D^{*-} decay is the same as in the data taken in 2000. This normalization is appropriate to extract qualitative information on the asymmetry. In the left panel the data exceed the calculated yields in the region $\Delta M \leq 0.17$ GeV, whereas in the right panel they are below the calculated values. This leads to the conclusion that the asymmetry is positive.

In the lower part of this figure the same comparison is made between the data and the ΔM spectrum calculated with PYTHIA, where the PYTHIA data are normalized by factor a of 2.2. In the ΔM region of 0.17-0.20 GeV the fraction of the data stemming from the decay of charmed mesons is found to be 8%. Hence, this part of the spectrum is expected to be dominated dominated by 'background' events. However, this region shows an unexpected and striking result.

In the domain $\Delta M = 0.17 - 0.20$ GeV, the number of events in the left panel (anti-parallel spins) is significantly smaller than the number of events from PYTHIA, and

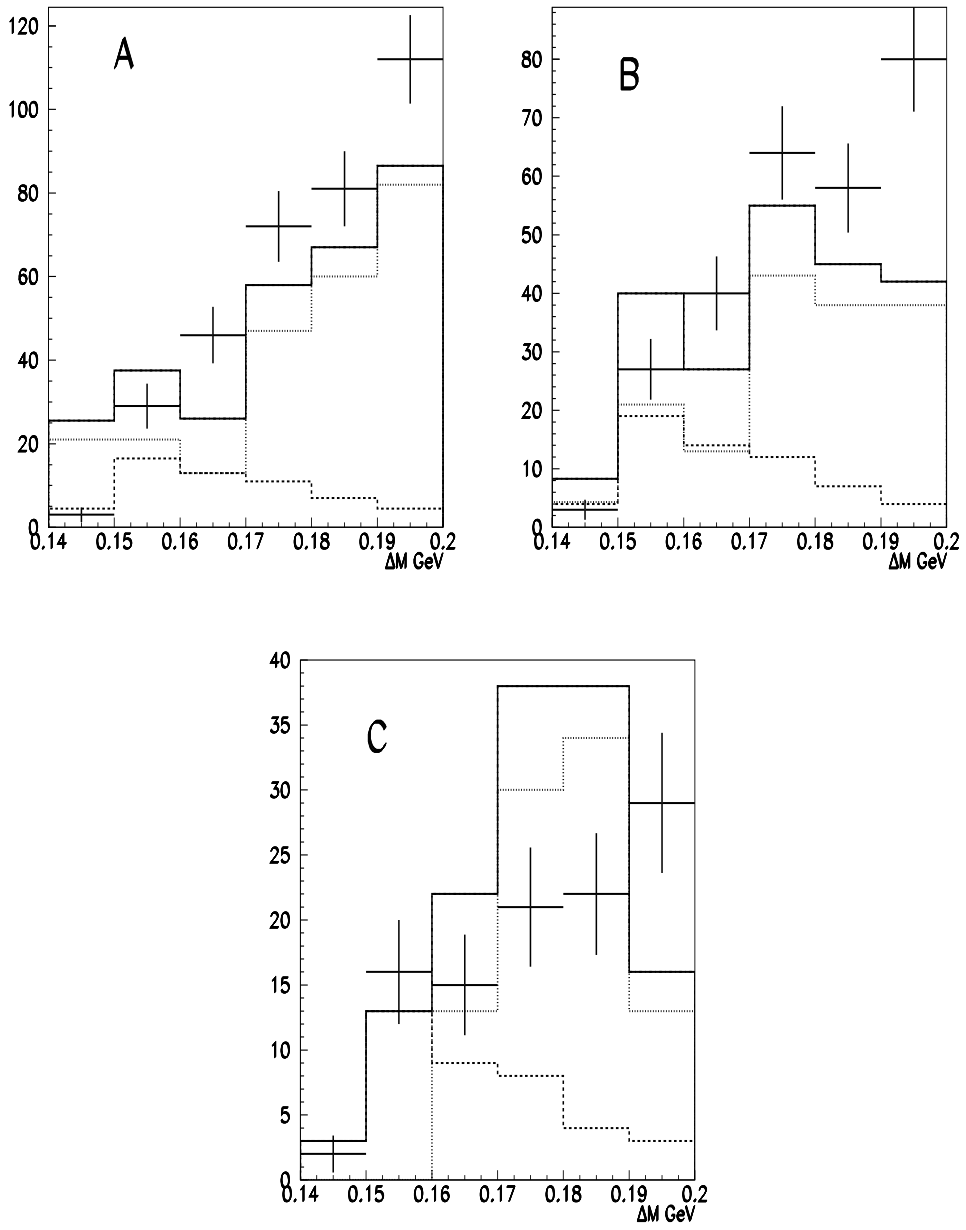

Figure 6.2: Results of fits (see table 6.1) of spectra calculated with the programs AROMA (dashed line) and PYTHIA (dotted lines) and the sum of two (solid line) to the ΔM spectra extracted from the data. Note the systematical increase of the fraction of events originating from D^{*-}-decay in the ΔM range 0.14 - 0.17 GeV.

in the right panel it is significantly larger. This indicates a large negative asymmetry, implying that another process (not involving charmed particles) must dominate the ΔM spectrum in this domain. At $\Delta M \geq 0.20$ GeV, the number of events in both panels is approximately equal.

In table 6.3 the data extracted from the measurements with target-spin parallel and anti-parallel to the helicity of the electrons are presented for the three intervals in ΔM (column 2 and 3). The data taken in 1999 and 2000 are added.

The double spin asymmetry for the production of charmed mesons is defined in equation (2.30). This asymmetry is related to the experimental asymmetry and can be rewritten in the number of events measured in the two directions of the target polarization normalized to the intergrated luminosity. Hence,

$$A_{\parallel}^{corrected} = \frac{A_{\parallel}^{exp}}{P_{target}P_{beam}}, \tag{6.7}$$

$$A_{\parallel}^{exp} = \frac{\frac{N_{\uparrow\Downarrow}}{L_{\uparrow\Downarrow}} - \frac{N_{\uparrow\Uparrow}}{L_{\uparrow\Uparrow}}}{\frac{N_{\uparrow\Downarrow}}{L_{\uparrow\Downarrow}} + \frac{N_{\uparrow\Uparrow}}{L_{\uparrow\Uparrow}}} = \frac{N_{\uparrow\Downarrow}L_{\uparrow\Uparrow} - N_{\uparrow\Uparrow}L_{\uparrow\Downarrow}}{N_{\uparrow\Downarrow}L_{\uparrow\Uparrow} + N_{\uparrow\Uparrow}L_{\uparrow\Downarrow}}. \tag{6.8}$$

The latter expression has been used to extract the double-spin asymmetries (table 6.3 column 4) with $\frac{L_{\uparrow\Downarrow}}{L_{\uparrow\Uparrow}} = 1.005$. In the last column this asymmetry is normalized to the target and beam polarization. The integrated value of $P_{target}P_{beam} = 0.47$ was used.

The asymmetry for the background is extracted from the data measured in the domain $\Delta M \geq 0.2$ GeV, where the contribution of D^{*-}-decay is negligible. This asymmetry is found to be zero.

In figure 6.4 the double-spin asymmetries extracted from the combined data sets obtained in 1999 and 2000 are displayed as a function of the fraction attributed to the decay of D^{*-}. This fraction F is obtained from fits to the data of the results from the Monte Carlo calculations listed in table 6.1 and defined as $F = \frac{charm}{sum} \times 100\%$ (see table 6.2). The data points at F=35 %, 52 % and 72 % correspond to the data in the range $\Delta M = 0.14 - 0.17$ GeV, and those for F=10 %, 17 % and 8 % to the ΔM range 0.17-0.20 GeV, for the cuts A, B and C, respectively. Note that they are obtained after the subsequent cuts on the kinematical variables, labeled as A, B and C in table 7. Therefore, the three values for one bin in ΔM are not independent. The data point at F=0 in the Fig. 6.4 reflects the asymmetry for the background (table 6.3 bottom part).

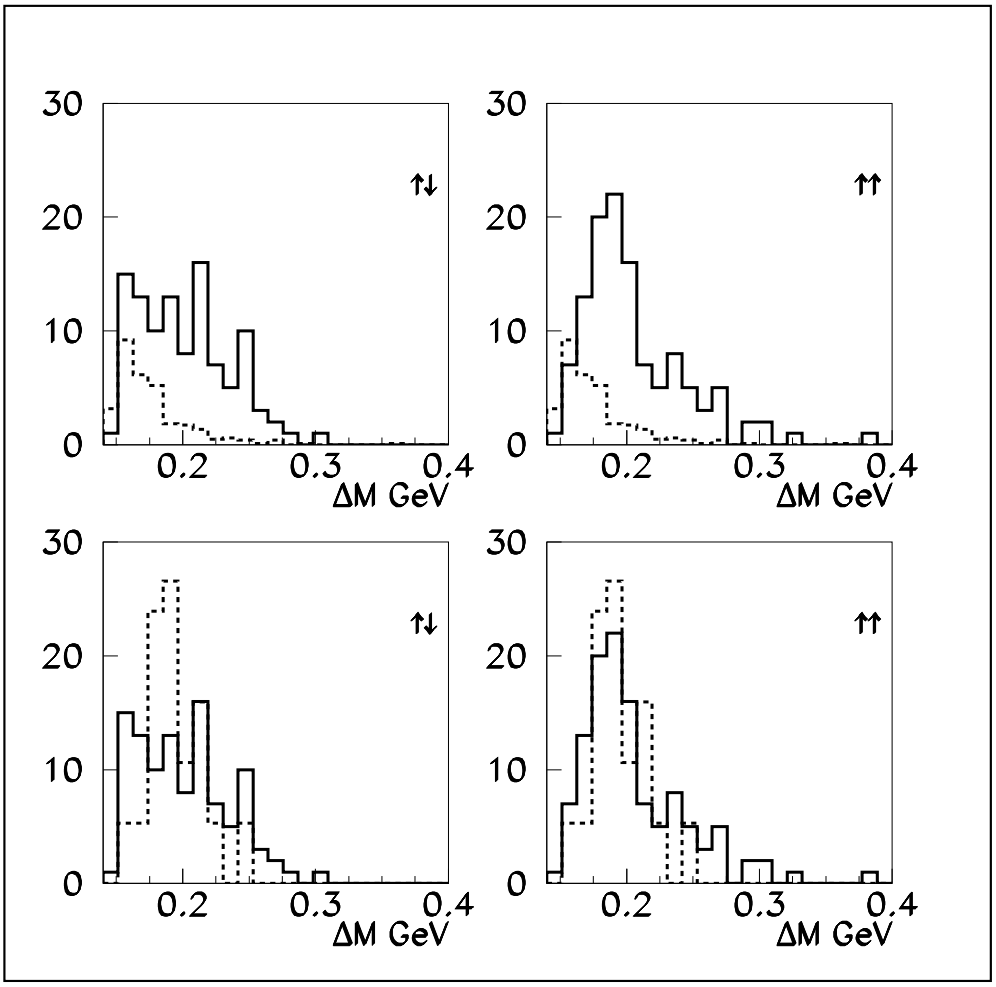

Figure 6.3: The ΔM spectra at two values of the beam-target polarizaton (solid histograms) compared with spectra (dashed histograms) calculated with AROMA (top) and PYTHIA (bottom).

ΔM = 0.14 - 0.17 GeV

	N_{events}		Asymmetry	
	$N_{\uparrow\Downarrow}$	$N_{\uparrow\Uparrow}$	$A_{\parallel}^{exp}$	$A_{\parallel}^{corrected}$
A	48	45	0.03±0.11	0.06±0.20
B	43	41	0.02±0.11	0.04±0.22
C	25	16	0.21±0.15	0.45±0.31

ΔM = 0.17 - 0.20 GeV

	N_{events}		Asymmetry	
	$N_{\uparrow\Downarrow}$	$N_{\uparrow\Uparrow}$	$A_{\parallel}^{exp}$	$A_{\parallel}^{corrected}$
A	138	177	-0.13±0.05	-0.26±0.11
B	97	134	-0.16±0.06	-0.33±0.13
C	31	52	-0.25±0.10	-0.53±0.22

ΔM = 0.2 - 1.6 GeV

	N_{events}		Asymmetry	
	$N_{\uparrow\Downarrow}$	$N_{\uparrow\Uparrow}$	$A_{\parallel}^{exp}$	$A_{\parallel}^{corrected}$
no	4562	4616	-0.01±0.01	-0.02±0.02

Table 6.3: Double-spin asymmetry measured for three ranges of the ΔM. Details are given in the text.

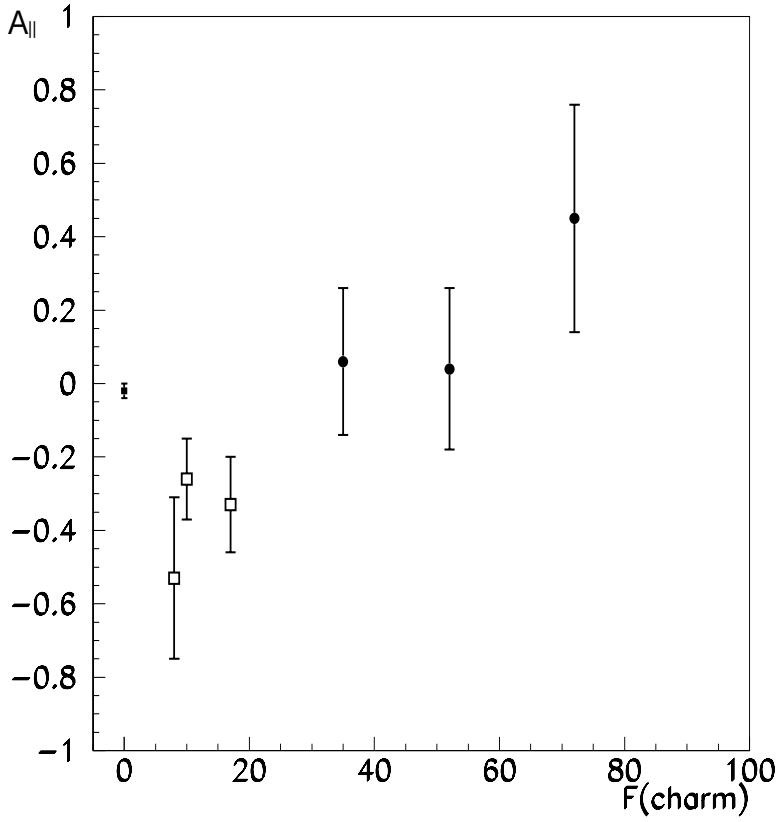

Figure 6.4: Asymmetry, corrected for the beam and target polarization as a function of the charm fraction for different ΔM ranges: $\Delta M = 0.14 - 0.17$ GeV (closed circles), $\Delta M = 0.17 - 0.20$GeV (squares) and $\Delta M > 0.20$ GeV (diamond).

6.3 Discussion

The asymmetries measured for both intervals in ΔM confirm the qualitative interpretation based on figure 6.3. In the first interval the asymmetry has a positive value of $A_{\parallel}^{corrected} = 0.45 \pm 0.31$ and in the second interval the asymmetry is negative, $A_{\parallel}^{corrected} = -0.53 \pm 0.22$. These observations have consequences for the extraction of the asymmetry for the creation of charmed mesons. Obviously, the assumption that the asymmetry stems from the decay of charmed mesons superimposed on a background with zero asymmetry is not correct, and the significant negative asymmetry in the ΔM range 0.17-0.20 GeV disturbs the anticipated regular increase of the asymmetry as a function of the charm fraction (F). This excludes a fit of a linear function to the seven values of $A_{\parallel}$ extracted from the data and an extrapolation of $A_{\parallel}$ to $F = 100$ %. Instead the smallest and largest values of $A_{\parallel}$ that are in accordance with the data

Decay product	Parent particle	Fraction
K^+	$K^{*0}(892)$ or $K^{*+}(892)$	95 %
π^-	$K^{*0}(892)$ or ω	40 %
e^-	π^0	100 %

Table 6.4: Events that contribute to the ΔM domain 0.17-0.20 GeV.

were estimated. The lower and upper limits of $A_\parallel$ at $F = 100$ % were estimated by discarding the processes that cause the negative asymmetry in the domain $\Delta M = 0.17$ - 0.20 GeV. A fit of a linear function to the four remaining data points and extrapolation to $F = 100$ % gives a value of $A_\parallel^{min} = 0.29 \pm 0.22$ (corrected for beam and target polarisation) at $F = 100$ %. Furthermore, an estimate of the maximum value of the asymmetry $A_\parallel^{max} = 0.51 \pm 0.44$ was obtained by fitting a linear function to the three data points corresponding to the domain $\Delta M = 0.14 - 0.17\,\mathrm{GeV}$ (c.f. Fig. 6.4), and subsequent extrapolation to $F = 100$ %. This gives for the lower and upper limits of the asymmetries the values of $A_\parallel^{lower} = 0.07$ and $A_\parallel^{upper} = 0.95$, respectively.

The upper limit of the asymmetry has no significance. From the value of $A_\parallel^{lower} = 0.07$ a lower value of $\frac{\Delta G}{G}$ was estimated. At the kinematic conditions of the HERMES experiment the average asymmetry $\hat{a}_{PGF}$ for creation of a $c\bar{c}$ in a photon-gluon-fusion reaction by completely polarized gluons is $\hat{a}_{PGF} = 0.6$ - 0.7 [19]. This gives a lower limit of $\frac{\Delta G}{G} \geqslant 0.1$ (See Eq. 2.30), and indicates that $\frac{\Delta G}{G}$ is positive.

A negative asymmetry $A_\parallel = -0.32 \pm 0.18$ was obtained by fitting a linear function to the three data points in the domain $\Delta M = 0.17 - 0.20\,\mathrm{GeV}$. As discussed above, the influence of the (unexpected) large negative asymmetry measured at in the range ΔM range 0.17-0.20 GeV hindered the extraction of $\frac{\Delta G}{G}$ from the data taken at ΔM = 0.17-0.20 GeV. On the other hand the measured negative asymmetry may open new windows to the determine the gluon polarization. For example a negative asymmetry can originate from strange mesons created in photon-gluon fusion. Therefore, it is of interest to study the origin of the e^-, K^+ and π^- particles that are responsible for the events in the ΔM domain 0.17-0.20 GeV. This information has been extracted from the calculations performed with PYTHIA. An inspection of the events that contribute to the ΔM domain 0.17-0.20 GeV gives the following results. 95 % of the kaons in this ΔM domain originate from the decay of $K^{*0}(892)$ or $K^{*+}(892)$ mesons, 40 % of the pions are emitted in the decay of a $K^{*0}(892)$ or ω meson, while 100 % of the electrons originate from π^0 decay (see table 6.4).

Figure 6.5 illustrates these findings. The solid histogram represents the ΔM spec-

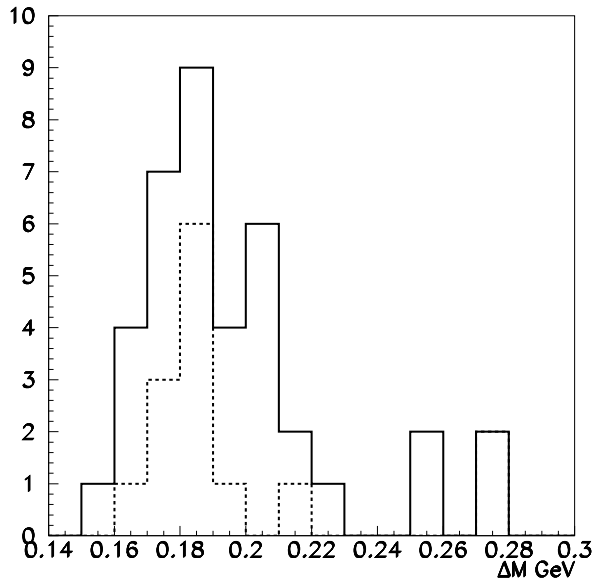

Figure 6.5: The ΔM for background generated with PYTHIA. The dashed histogram - extra conditions on the parents of the decay products.

trum calculated with PYTHIA, after applying the three steps in the data reduction (this is the same spectrum as displayed on the bottom part of Fig. 6.3 as a dashed histogram). The dashed histogram is obtained by requiring in addition that the e^- and K^+ are decay products from the particles mentioned above; no condition on π^- is set , because this particle can originate from the decay of various particles. Note that the shape and the width of the two spectra in the ΔM range 0.17 - 0.20 GeV is similar, and that these particles account for about 50% of the total number of events in this ΔM spectrum.

From this information a few decay paths can be reconstructed. For example, the parent is a $K^{*0}(892)$ or K^{*0} with an energy of 1410 MeV, 1430 MeV or larger and decays into

$$K^{*0}(892) + \pi^0 \rightarrow \pi^- + K^+ + e^-(e^+) \text{ or}$$
$$\omega(782) + K^+ \rightarrow \pi^- + \pi^+ + K^+ + e^-(e^+) \; .$$

These decays are illustrated in the Fig. 6.6.

Thus far, the procedure followed in the data analysis was to enhance the contribution of events from D^{*-}-decay in the mass and mass-difference spectra. At first view

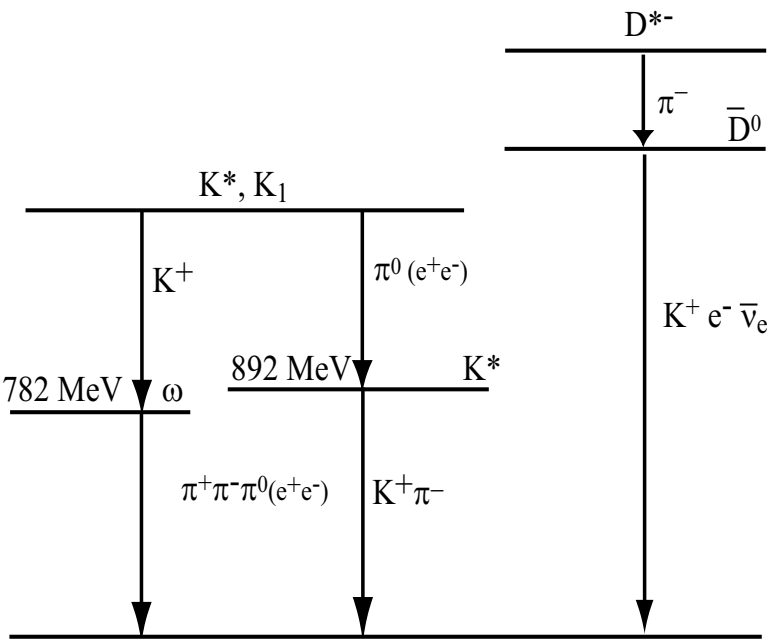

Figure 6.6: The decay of strange mesons K^* in comparison with the decay of D^{*-}-mesons when the same final state particles are detected.

it is surprising that in this ΔM spectrum a small peak shows up from a decay process for which this ΔM has no meaning. The explanation for this observation is found in the formula $\Delta M = M(\pi^- K^+ e^-) - M(K^+ e^-)$. Independent of the decay process ΔM has a small value when the pion momentum is small. In the decay $D^{*-} \rightarrow \bar{D^0}, \pi^-$ the pion momentum is only 0.041 GeV when the D^{*-} has zero momentum. Therefore, the ΔM spectrum for the decay of this particle has a maximum slightly above the pion mass. In the decay of a $K^*(892)$ at rest the maximum pion momentum is 0.286 GeV, which is small in comparison to the momenta of the particles in the laboratory frame. This explains the peak at 0.18 GeV in ΔM.

To study the decay processes shown in figure 6.6 in more detail an appropriate data reduction has to be applied to reduce the background. This reduction should be based on the selection of the same particles as in the analysis of the D^{*-} decay, but starting from the invariant mass $M(K^+\pi^-)$ and requiring in addition that an e^- is emitted by the π^0. Figure 6.7 shows this calculated $M(K^+\pi^-)$ spectrum. As in the analysis of the Monte Carlo data for the D^{*-} decay, conditions were set on the electron momentum (1.5 GeV) and the kaon momentum (2 GeV). Events in which the electron is emitted in the decay of a π^0 meson show a sharp peak around the mass of the $K^*(892)$. The spectrum of the remaining events gradually decreases with inrease of $M(K^+\pi^-)$. This

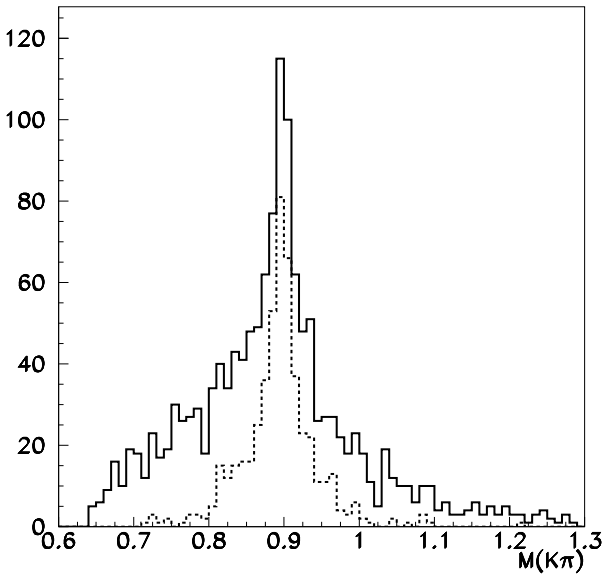

Figure 6.7: Calculated M($K^+\pi^-$) spectrum. Dashed line - e^- emitted from π^0, K^+ and π^- from $K^*(892)$. Solid histogram indicates all events.

indicates that the selected particles likely correspond to the decay of K^* and K mesons in the domain $1.3 - 1.7$ GeV as shown in Fig. 6.6.

The prominent peak in the calculated $M(K^+\pi^-)$ spectrum offers good prospects for a more detailed Monte-Carlo study, similar as for the D^{*-} decay, to further reduce the background. Then, the existing set of data (events with one π^0, one K^+ and one e^-) can be analysed applying conditions extracted from the Monte-Carlo calculations.

The spectrum shown in figure 6.7 allows already to make an estimate of the number of events that one may expect in the $M(K^+\pi^-)$ spectrum extracted from the data. From the comparison of the calculated $\Delta M = M(\pi^- K^+ e^-) - M(K^+ e^-)$ spectrum to the data (Figure 6.1) a normalization factor $N = 4.4$ was extracted (Table 6.1). Applying this factor to the calculated $M(K^+\pi^-)$ spectrum results in about 380 events in the peak (0.85 GeV $\leq \mathrm{M_{K\pi}} \leq$ 0.95 GeV) and about 700 events in the total spectrum. This allows an accurate determination of the double-spin asymmetry.

Chapter 7

Summary

Measurements of the double-spin asymmetry in deep-inelastic electron scattering on a proton and a deuteron have shown that the valence quarks account for only about 20 % of the nucleon spin. This observation suggests an important contribution to the nucleon spin from gluons and/or the orbital angular momentum.

Information on the contribution of the gluons to the nucleon spin can be obtained from the cross-section asymmetry for photon-gluon fusion (PGF) induced by longitudinally polarized leptons on a longitunal polarized target nucleon. In this process a $q\bar{q}$ pair is created and possibly one or more gluons of smaller energy. The $q\bar{q}$ pair most likely fragments into two mesons of opposite charge. It is also possible that the quark created in the PGF reaction and two quarks from the target nucleon form a baryon. In the latter process also two mesons are created, one of which contains the anti-quark created in the PGF process.

At the electron-beam energy of 27 MeV provided by HERA and the fixed target used in HERMES experiment the maximum centre-of-mass energy of the positron-nucleon system is about 7 GeV. This implies that the momenta of the created hadrons in the centre-of-mass system of the virtual photon and the nucleon strongly depend on the mass of the quarks involved. Hadrons created in a PGF reaction involving valence quarks generally have a large transverse momentum, whereas this momentum is small for charmed hadrons. This is because the invariant energy of the electron(positron)-nucleon system is close to the threshold for creation of a $c\bar{c}$ pair.

In previous studies on the decay of charmed hadrons within the HERMES collaboration, the cross-sections for the production of J/Ψ, D^*, D mesons and the Λ_c baryon were measured. It was shown in these studies that the cross sections for creating charmed particles at an electron energy of 27 MeV are small. Futhermore, it was observed that the background in the reconstructed mass and mass-difference spectra

is large and strongly depends on the decay mode of the created particles.

This thesis reports on a study of the semi-leptonic decay of D^{*-} mesons produced in the interaction of quasi-real photons with the target nucleons. This decay is as follows: $D^{*-} \to \bar{D}^0\pi^- \to K^+e^-\bar{\nu}_e\pi^-$.

The advantage of this decay-channel as compared to the hadronic decay is the presence of the electron. This particle is not frequently produced at the energies of the HERMES experiment, if a positron beam is used. However, the antineutrino $\bar{\nu}_e$ cannot be observed. As a consequence the mass of the D^{*-} meson can be only partially reconstructed. This implies a large width of the reconstructed mass. Therefore, the asymmetry is determined using the mass-difference spectrum $\Delta M = M_{D^{*-}} - M_{\bar{D}^0\pi^-}$. In this spectrum the effect of the non observation of the $\bar{\nu}_e$ is largely removed.

First, Monte-Carlo calculations were performed to study the ΔM spectrum and the background. The creation and decay of D^{*-} mesons was simulated with the program AROMA and the events which contribute to background with the program PYTHIA. Using these Monte-Carlo data, selection criteria were developed and applied to the data in order to reduce the background with a minimum reduction of events from D^{*-}-decay. They include constraints to the momenta p_{K^+}, p_{π^-}, p_{e^-} and to the sum of p_{K^+} and p_{e^-}. Furthermore, constraints were set to the emission angles of the electron and kaon relative to the pion momentum. These angles are small for events from the $D^{*-} \to \pi^-$ $\bar{\mathrm{D}}^0 \to \pi^-e^-K^+$ $(\bar{\nu}_e)$ decay. Finally, the correlations between the reconstructed mass of the $\bar{\mathrm{D}}^0$ versus the pion momentum were used to decrease the background in the ΔM spectrum.

According to the results of the Monte-Carlo calculations the background due to the decay of non-charmed mesons is reduced to 0.3% of the initial number of events while this reduction is only 47% for events from D^{*-}-decay.

The selection criteria extracted from the Monte-Carlo calculations were applied to the data taken in 1999 and 2000. Both data sets were analyzed separately. The target in these two years was polarized deuterium. First, the ranges in the momenta of the particles involved were reduced and it was required that the minimum distances between K^+, e^- and π^- tracks within the target are ≤ 1 cm. Then, the various selection ctiteria mentioned above were applied.

To extract the number of events from D^{*-}-decay, the Monte-Carlo data were fitted to the measured ΔM spectrum. The fits were performed with two parameters, a normalization constant and the fraction of the events from D^{*-}-decay. The fits were performed at each step of the data analysis.

According to these fits the fraction of the events from D^{*-}-decay in the selected

domain of $\Delta M = 0.14 - 0.17$ GeV is 72% if all requirements are imposed, while in the ΔM range of $0.17 - 0.20$ GeV this fraction is only 8%.

Double-spin asymmetries have been extracted from the data in the two domains of ΔM mentioned above. They are corrected for beam and target polarization. The double-spin asymmetry measured in the ΔM range $0.14 - 0.17$ GeV is $A_{\parallel}^{corrected} = 0.45 \pm 0.31$. Whereas in the domain $\Delta M = 0.17 - 0.20$ GeV, where background dominates the spectrum, this asymmetry has a sizeable negative value of $A_{\parallel}^{corrected} = -0.53 \pm 0.22$.

The negative asymmetry of the background likely contributes to the asymmetry in the ΔM range 0.14-0.17 GeV as well. This effect and the large statistical uncertainty in the double-spin asymmetry in the ΔM region of interest do not allow a reliable extraction of the gluon polarization from the data.

A simulation of the events in the ΔM range 0.17-0.20 GeV performed with PYTHIA, showed that the events in this domain mainly originate from $K^{*0}(892)$ decay, with a sizeable contribution from the decay of the $\omega(792)$-meson. Furthermore, the electrons stem from π^0 decay. Hence, possible decay channels associated with the predictions of these mesons are

$$K^{*0}(892) + \pi^0 \rightarrow \pi^- + K^+ + e^- + e^+ \quad \text{or}$$
$$\omega(782) + K^+ \rightarrow \pi^- + \pi^+ + e^- + e^+ + K^+ \, .$$

Wherein, according to PYTHIA the $K^{*0}(892)$ and π^0 seem to originate from the decay of a $K^{*0}(1410)$, $K^{*0}(1430)$ or heavier K^*-mesons.

A dedicated study of the double-spin asymmetry for the events containing the same particles but requiring an invariant mass $M_{K^+\pi^-}$ corresponding to the $M_{K^{*0}(892)}$ mass may open a window to investigate the origin of the large negative asymmetry observed in the ΔM range betveen 0.17 and 0.20 GeV. As PYTHIA suggests that a sizeable fraction of the heavy K^{*0} mesons mentioned above is produced through PGF, these large negative asymmetry might even be used to study the gluon polarization. A preliminary analysis of this decay channel based on the reconstruction of the invariant mass $M(K^+\pi^-)$ shows a clear peak at $M = 892$ MeV, and contains about 700 events with a significant negative asymmetry. This gives good prospects for a more detailed analysis.

Chapter 8

Samenvatting

Metingen van de tweevoudige spin-asymmetrie in diep-inelastische elektronenverstrooiing aan een proton en een deuteron hebben aangetoond dat de valentiequarks slechts ongeveer 20% bijdragen aan de spin van het nucleon. Deze waarneming suggereert een belangrijke bijdrage aan de nucleonspin van de gluonen en/of het baanimpulsmoment.

Informatie over de bijdrage van de gluonen aan de nucleonspin kan worden verkregen uit de asymmetrie van de werkzame doorsnede voor foton-gluon fusie (PGF) geïnduceerd door longitudinaal gepolariseerde leptonen aan een longitudinaal gepolariseerd nucleon. In dit proces wordt een $q\bar{q}$ paar gevormd en mogelijk één of meer gluonen met minder energie. In de meeste gevallen fragmenteert het $q\bar{q}$ paar in twee mesonen met tegengestelde lading. Het is ook mogelijk dat het quark dat is gevormd in de PGF reactie en twee quarks van het getroffen nucleon een baryon vormen. In dit laatste proces worden ook twee mesonen gevormd, waarvan één het anti-quark bevat dat gecreëerd is in het PGF proces.

In een reactie tussen positronen met een energie van 27 GeV, die door HERA wordt geleverd, met nucleonen in een gascel, die wordt gebruikt in het HERMES experiment, is de maximale energie in het massamiddelpunt van het positron-nucleon systeem ongeveer 7 GeV. Dit betekent dat de impulsen van de geproduceerde hadronen in het massamiddelpuntsysteem van het virtuele foton en het nucleon sterk afhangen van de massa van de betrokken quarks. Hadronen die zijn geproduceerd in een PGF reactie waarbij valentie quarks zijn betrokken hebben in het algemeen een grote transversale impuls, terwijl die component van de impuls klein is voor hadronen met 'charm'. Dit komt doordat de invariante energie van het positron-nucleon systeem dicht bij de drempelwaarde ligt voor de creatie van een $c\bar{c}$ paar.

In voorgaande studies van het verval van hadronen met charm in de HERMES collaboratie zijn de werkzame doorsneden gemeten voor de productie van J/Ψ, D^*, D

mesonen en het Λ_c baryon. In deze studies is aangetoond dat de werkzame doorsneden voor het maken van deeltjes met charm bij een energie van 27 GeV klein zijn. Ook heeft men waargenomen dat de achtergrond in de gereconstrueerde massa en massaverschil spectra groot is en sterk afhangt van het verval van de gecreëerde deeltjes.

Dit proefschrift beschrijft een studie van het semi-leptonische verval van D^{*-} mesonen die zijn geproduceerd in de wisselwerking van quasi-reële fotonen met nucleonen. Dit verval is als volgt: $D^{*-} \rightarrow \bar{D}^0\pi^- \rightarrow K^+e^-\bar{\nu}_e\pi^-$.

Het voordeel van dit vervalkanaal vergeleken met het hadronische verval is de aanwezigheid van het elektron. Productie van een elektron met hoge energie heeft geen grote waarschijnlijkheid in het HERMES experiment, waar een positronbundel wordt gebruikt. Echter het anti-neutrino, $\bar{\nu}_e$, kan niet gemeten worden. Een consequentie hiervan is dat de massa van het D^{*-} meson slechts gedeeltelijk kan worden gereconstrueerd. Dit impliceert een grote breedte van het gereconstrueerde massaspectrum. Om deze reden wordt de asymmetrie bepaald met behulp van het massaverschil spectrum $\Delta M = M_{D^{*-}} - M_{\bar{D}^0\pi^-}$. In dit spectrum wordt het effect van het niet gemeten neutrino voor een groot deel ongedaan gemaakt.

Als eerste zijn Monte-Carlo simulaties uitgevoerd om het ΔM spectrum en de achtergrond te bestuderen. De productie en het verval van D^{*-} mesonen zijn gesimuleerd met het programma AROMA en de gebeurtenissen die een bijdrage leveren aan de achtergrond met het programma PYTHIA. Gebruikmakend van deze gesimuleerde spectra zijn selectiecriteria ontwikkeld en toegepast op de meetgegevens om de bijdrage van de achtergrond te verkleinen met een minimaal verlies van gebeurtenissen van D^{*-} verval. Deze bevatten beperkingen van de impulsen p_{K^+}, p_{π^-}, p_{e^-}, en op de som van p_{K^+} en p_{e^-}. Voorts zijn er beperkingen opgelegd aan de hoeken waaronder het elektron en het kaon ten opzichte van de pion-impuls worden uitgezonden. Deze hoeken zijn klein voor het $D^{*-} \rightarrow \pi^-\ \bar{\mathrm{D}}^0 \rightarrow \pi^-e^-K^+\ (\bar{\nu}_e)$ verval. Als laatste zijn correlaties tussen de gereconstrueerde massa van de $\bar{\mathrm{D}}^0$ meson en de pion-impuls gebruikt om de achtergrond in het ΔM spectrum te verkleinen.

De resultaten van de Monte-Carlo berekeningen laten zien dat door deze bewerkingen de achtergrond, veroorzakt door het verval van mesonen zonder charm, gereduceerd wordt tot 0.3% van het initiële aantal gebeurtenissen, terwijl deze verkleining slechts 47% is voor de gebeurtenissen afkomstig van het D^{*-} verval.

De selectie criteria, verkregen uit de Monte-Carlo berekeningen, zijn toegepast op de meetresultaten van 1999 en 2000. Beide zijn afzonderlijk geanalyseerd. In deze jaren werd gepolariseerd deuterium als "trefplaat" gebruikt. In de analyse van de meetgegevens werd als eerste het bereik in de impuls van de deeltjes verkleind en werd

vereist dat de minimum afstand tussen de K^+, e^- en π^- sporen binnen de "trefplaat" kleiner is dan 1 cm. Vervolgens werden de bovengenoemde selectiecriteria toegepast.

Om het aantal gebeurtenissen te bepalen dat afkomstig is van het D^{*-} verval, werden de Monte-Carlo spectra aangepast aan de gemeten ΔM spectra. Deze vergelijking werd uitgevoerd met twee parameters, een normalisatie constante en de fractie van de gebeurtenissen van het D^{*-} verval, voor elke stap van de analyse van de meetgegevens.

Volgens deze analyse is de fractie van gebeurtenissen van D^{*-} verval in het uitgekozen domein van $\Delta M = 0.14 - 0.17$ GeV gelijk aan 72% als alle selectie eisen worden toegepast, terwijl in een ΔM domein van $0.17 - 0.20$ GeV deze fractie slechts 8% is.

Uit de meetresultaten voor de twee genoemde ΔM domeinen is de tweevoudige spin-asymmetrie bepaald. Deze zijn gecorrigeerd voor polarisatie van de positronen en de 'treftplaat' nucleonen. De gemeten tweevoudige spin-asymmetrie in het ΔM domein $0.14 - 0.17$ GeV is $A_{\parallel}^{gecorrigeerd} = 0.45 \pm 0.31$. Terwijl in het domein $\Delta M = 0.17 - 0.20$ GeV, waar de achtergrond het spectrum overheerst, de asymmetrie de aanzienlijke negatieve waarde heeft van $A_{\parallel}^{gecorrigeerd} = -0.53 \pm 0.22$.

De negatieve asymmetrie van de achtergrond draagt waarschijnlijk ook bij aan de asymmetrie in het ΔM gebied $0.14 - 0.17$ GeV. Dit effect en de grote statistische onzekerheid in de tweevoudige spin-asymmetrie in het interessante ΔM gebied staan niet toe dat er een betrouwbare waarde van de gluonpolarisatie uit de meetresultaten wordt verkregen.

Een simulatie van de gebeurtenissen in het ΔM gebied van 0.17-0.20 GeV, uitgevoerd met PYTHIA, laat zien dat de gebeurtenissen in dit domein voor het grootste gedeelte afkomstig zijn van het $K^{*0}(892)$ verval, met een aanzienlijke bijdrage van het verval van het $\omega(792)$-meson. Voorts worden de elektronen in het π^0 verval uitgezonden. Hieruit volgen als mogelijke vervalskanalen voor deze mesonen,

$$K^{*0}(892) + \pi^0 \rightarrow \pi^- + K^+ + e^- + e^+ \quad \text{en}$$
$$\omega(782) + K^+ \rightarrow \pi^- + \pi^+ + e^- + e^+ + K^+ ,$$

waarbij, volgens PYTHIA, de $K^{*0}(892)$ and π^0 mesonen afkomstig blijken te zijn van het verval van het $K^{*0}(1410)$, $K^{*0}(1430)$ of zwaardere K^* mesonen.

Een gerichte studie van de tweevoudige spin asymmetrie voor de gebeurtenissen die dezelfde deeltjes bevatten maar met een invariante massa $M_{K^+\pi^-}$ overeenkomend met de $M_{K^{*0}}(892)$ massa hebben, kan een venster openen om de herkomst van de grote negatieve asymmetrie, die wordt waargenomen in het ΔM gebied tussen 0.17 en

0.20 GeV, te onderzoeken. Omdat PYTHIA suggereert dat een aanzienlijk deel van de bovengenoemde K^{*0} mesonen met grote massa geproduceerd wordt in foton-gluon fusie, kunnen deze grote negatieve asymmetrieën zelfs gebruikt worden om de gluon-polarisatie te bestuderen. Een voorlopige analyse van dit vervalskanaal, gebaseerd op de reconstructie van de invariante massa $M(K^+\pi^-)$, laat een duidelijke piek zien bij $M = 892$ MeV, en bevat ongeveer 700 gebeurtenissen met een significante asymmetrie. Dit geeft goede vooruitzichten voor een meer gedetailleerde analyse.

Acknowledgements

Finally, I am getting to the end of this manuscript. Many people have influenced my life during my work here and I would try to mention all of them.

Dear Willem, without your help and support that I was receiving at all stages of my work and life this thesis would have never been completed. Hours and hours of very fruitful discussions, which we had, were very productive. Especially I would like to mention the vertex reconstruction algorithm that was used in the analysis. Thank you very much!

I am giving my great respect to my promoter. Dear Jo, thank you for all your efforts and help including very important advice on my work and the thesis itself.

Dear Gerard, for me you are a unique example of a very good group-leader and great scientist. There was no question that you did not answer, and all your comments were extremely useful. Thanks a lot for everything!

I would like to thank Jos and Keith for very important discussions on the analysis I was working at.

My kind regards to Teus van Egdom and Ed van Willigen for the help I was constantly receiving from the Personnel Department.

I want to say special thanks to Julian Budagov, for the great research experience that I received while working in the department of Multiple Hadronic Processes in the JINR (Russia).

As this thesis was (an is) a part of my life, my friends had a big influence on it. I want to say thank you to my old friends Peter Hofmann-Rothe, David Heesbeen, Johan Blow, Jan Visser, Andreas Reischl, Vanessa Mexner, Jeroen van Hunen and Chiara Simani. They were the people I started to work and (which is also very important) to explore Amsterdam with. One could hardly find a bar downtown Amsterdam where we were never been and (special thanks to Erika and Chiara). I still remember by names all the pizzerias that we have visited and I am still having problems with Chianti.

I want to say kind words about friends and colleagues that joined our group later.

Thanks to Gabriel Ybeles Smit without his calculations this thesis would not be

completed!

Thanks to Jeroen Dreschler, Vladas Tvaskis (for very nice advice on LATEX) and to Paul van der Nat.

Special thanks to Maxim Geerts for being such a great friend!

The amount of beer we consumed while talking is incredible and so be it! And perspectives always appear, my friend! :)

And to my family, indeed this thesis was written for them. And without the support I was constantly receiving from them I would have never finished my research.

To my father Eduard Laziev, to my mother Anelia Hasratian, to my brother Mike (Mkrtich), his wife Tamara and my niece Eve and, of course, to my lovely Yulia and little Sonja! Thank you very much, I love you all a lot!!!

Amsterdam...one of the reasons why I applied for this position was You, I liked You from the very first look and I still like You very much. Your cosy streets and pubs bring up lot of good memories, thank You.

This book is completed; with this book an important part of my life is ending. It is time to turn the last page and to move ahead.

Bibliography

[1] M. Gell-Mann. A schematic model of baryons and mesons. *Phys. Lett., 8 (1964) 214.*

[2] G. Zweig. An SU(3) model for strong interaction symmetry and its breaking. *Technical report, CERN-TH-412, (1964).*

[3] J. D. Bjorken. Asymptotic sum rules at infinite momentum. *Phys. Rev., 179, (1969) 1547.*

[4] J. Ashman et al. *Phys. Lett. B 206, (1998) 364.*

[5] R. L. Jaffe. *MIT-CTP-2466, hep-ph/9509279.*

[6] T. K. Gehrmann and W. J. Stirling. *Phys. Rev. D53, (1996) 610.*

[7] F. Meisner. *HERMES internal report, 98-051, (1998).*

[8] E. Volk. Measurement of the $D^{*\pm}$ Cross-Section at HERMES. *PhD Thesis. Ruprecht-Karls-Universitaet. Heidelberg. Germany, (2001).*

[9] S. Brons. Analysis of $D^{*+} \rightarrow \pi^+ D^0$ and $D^{*-} \rightarrow \pi^+ D^0$ in the 1996-1997 HERMES data. *Internal Report. HERMES, 98-057, (1998).*

[10] D. Heesbeen. Quasi-Real photo-production of hyperons on polarized $^{1,2}H$ targets. *PhD Thesis, Rijksuniversiteit Groningen, (2003).*

[11] E. Leader and E. Predazzi. An introduction to gauge theories and the new physics. *Cambridge Univ. Press, (1982).*

[12] A. Efremov M. Anselmino and E. Leader. The theory and phenomenology of polarized deep-inelastic scattering. *Phys. Rep. (1982) 1.*

[13] W. K. H. Panofski. Electromagnetic interactions: low Q^2 electrodynamics, elastic and inelastic electron and muon scattering. *In Proc. of the 14-th Int. Conf. of High Energy Physics. Vienna, (1968).*

[14] M. Breidenbach et al. Observed behaviour of highly inelastic electron-proton scattering. *Phys. Rev. Letter., 23, (1969) 935.*

[15] J. D. Bjorken. Asymptotic sum rules at infinite momentum. *Phys. Rev., 179, (1969) 1547.*

[16] J. D. Bjorken and E. A. Paschos. Inelastic electron-proton and gamma-proton scattering and the structure of the nucleon. *Phys. Rev., 185, (1969) 1975.*

[17] R. P. Feynman. Photon-hadron interactions. *Benjamin, Reading, MA, (1972).*

[18] M. C. Simani. Flavour decomposition of the nucleon spin at HERMES. *PhD Thesis, Vrije Universiteit, Amsterdam, (2002).*

[19] K. Kurek A.Bravar and R. Windmolders. POLDIS a Monte Carlo for POLarized (semi-inclusive) Deep Inelastic Scattering. *Comput.Phys.Commun. 105, (1997) 42-61.*

[20] I. Schmidt C. Peterson, D. Schlatter and P. M. Zerwas. Scaling violations in inclusive e^+e^- annihilation spectra. *Phys. Rev., D 27, (1982) 105-111.*

[21] A. A. Sokolov and I. M. Ternov. *Sov. Phys. Dokladi 8, (1964) 1203.*

[22] M. Ryskin and E. Leader. Contamination of spin asymmetry in charm production. *J. Physics. G25, (1999) 1541-1543.*

[23] C.Y. Scarlett. Photon-Gluon fusion as a way of accessing the gluons' contribution to nucleon spin. *Dissertation,University of Michigan, (2002).*

[24] T. Sjostrand. AROMA 2.2. *Computer Physics Commun., (1994) 82.*

[25] T. Sjostrand et al. PYTHIA 6.2 Physics and manual. *DESY note, (2001).*

[26] Ingelman et al. AROMA 2.2 a Monte-Carlo Generator for Heavy Flavour Events in *ep* Collisions. *DESY note, 058, (1996).*

[27] Ingelman et al. LEPTO 6.5 a Monte-Carlo Generator for Deep-Inelastic Lepton-Nucleon Scattering. *DESY note, 057, (1996).*

[28] T. Sjostrand et al. PYTHIA 6.2. *Computer Physics Commun.,135, (2001), 238.*

[29] W. Wander. Reconstruction of High Energy Scattering Events in the HERMES Experiment. *PhD Thesis (English version), (1997).*

[30] P. Bailey and N. Makins. Search for the semi-leptonic decay $D^{*-} \rightarrow K^+e^-\pi^-X$. *HERMES Internal Report, (2002).*

[31] D. P. Barber et al. The HERA polarimeter and the first observation of electron spin polarization. *Nucl. Instr. Meth., A338, (2000) 21.*

[32] M. Dueren. The HERMES experiment: From the design to the first results. *Habilitation thesis. Germany. (1995).*

[33] P. Oelwein. Messung der longitudinalen Electronenpolarization beim Speicherring HERA und Monte-Carlo Studien zur Kalibration des HERA-Electronen-Polarimeters. *Diploma Thesis. Max-Planck-Institut Germany, (1995).*

[34] M. Beckmann et al. The longitudinal polarimeter at HERA. *Nucl. Instr. Meth., A461, (2000) 21.*

[35] N. Koch. A study of the production of intense cold atomic beams for polarized hydrogen and deuterium targets. *PhD Thesis. Friedrich-Alexander Univ. Erlangen, (1999).*

[36] C. Baumgarten et al. An atomic beam polarimeter to measure the nuclear polarization in the HERMES gaseous polarized hydrogen and deuterium target. *DESY-01-078, (2001).*

[37] HERMES collaboration. HERMES technical design report. *DESY-PRC-93-06, (1993).*

[38] D. Ryckbosch. The HERMES RICH detector. *Nucl. Instr. Meth., A433, (1999) 98-103.*

[39] R. C. Fernow. *Brookhaven Nat. Lab. Preprint. BNL-42114, (1998).*

[40] H. R. Avakian et al. The HERMES electromagnetic calorimeter. Prepared for 6th International Conference on Calorimetry in High-Energy Physics. *ICCHEP 96, Rome, Italy, (8-14 June 1996).*

[41] H. R. Avakian et al. Performance of the electromagnetic calorimeter of the HERMES experiment. *Nucl. Instr. Meth., A417, (1998), 69-78.*

[42] N. Akopov et al. The HERMES dual-radiator ring imaging Čerenkov detector. *Nucl. Instr. Meth., A479, (2002) 511-530.*

[43] K. Negodaeva. The PID efficiency of the RICH IRT method. *HERMES Internal Note/00-026, (2002).*

[44] R. Kaiser. Likelihood analysis for the RICH IRT method. *Internal report. HERMES 00-016, (2000).*

[45] T. Benisch et al. The luminosity monitor of the HERMES experiment at HERA. *HERMES, (2000).*

[46] M. Ehrenfried. Eine Studie zur Nachweisbarkeit von open-charm-Ereignisses bei HERMES. *Master thesis. Westfaelische Wilhelms-Universitaet. Munster. Germany, (2001).*

[47] M. Ehrenfried. E. C. Aschenauer. Open charm in 1997 polarized data? *HERMES Internal Report. 01-028, (2001).*

[48] P. L. Anthony et al. *Phys. Rev. D 54, (1996) 6620.*

[49] K. Abe et al. *Phys. Rev. Lett. 79, (1997) 26.*

[50] P. L. Anthony et al. *Phys. Lett. B 463, (1999) 339.*

[51] B. W. Filippone et al. *hep-ph/0101224.*

[52] R. Hofstadter. Electron scattering and nuclear and nucleon structure. *W. A. Benjamin, INC., N.Y., (1963).*

[53] M. A. Funk. A measurement of the polarized parton densities of the nucleon in deep inelastic scattering at HERMES. *DESY-Thesis-1998-017, (1998).*